Towards optical diagnostics and control in aerotaxy semiconductor nanowire growth

Samuelsson, Per

2021

Towards optical diagnostics and control in aerotaxy semiconductor nanowire growth

Towards optical diagnostics and control in aerotaxy semiconductor nanowire growth

by Per Samuelsson

LUND
UNIVERSITY

Thesis for the degree of Doctor of Philosophy
Thesis advisors: Prof. Zhongshan Li, Prof. Marcus Aldén

Faculty opponent:
Prof. Mark Linne, School of Engineering, University of Edinburgh, UK

To be presented, with the permission of the Faculty of Engineering of Lund University, for public criticism in the Rydberg hall (Rydbergsalen) at the Department of Physics on Thursday, the 27th of May 2021 at 13:15.

Organization
LUND UNIVERSITY

Department of Physics
Box 118
SE–221 00 LUND
Sweden

Document name
DOCTORAL DISSERTATION

Date of disputation
2021–05–27

Sponsoring organization

Author(s)
Per Samuelsson

Title and subtitle
Towards optical diagnostics and control in aerotaxy semiconductor nanowire growth

Abstract

Aerosol growth of semiconductor nanowires has the potential to dramatically lower the cost of for solar cell production. The objective of the work was to study the growth of aerosol nanoparticles and nanowires, in order to understand the chemical and physical processes involved. This was accomplished by studying the early parts of growths using optical diagnostic techniques. The work involved developing a platform providing the chemical environment enabling in-situ measurements, as well as developing the necessary optical and spectroscopic techniques. The thesis contains two main parts. The first part concerns optical measurements in a spark discharge for generation of gold nanoparticles that acts as seeds for nanowire growth. A discharge system was designed which produces metal nano-aerosols by condensation of atomic vapor ablated from the gold electrodes. The discharge system was characterized electrically, and ex-situ with respect to the particles generated. A laser triggering scheme was developed, enabling synchronization of the self-pulsing discharge to a pulsed probe laser. The discharge plasma was studied using a combination of broadband emission spectroscopy, pulsed laser-induced fluorescence, and high-resolution absorption spectroscopy in a spatially and temporally resolved manner. In order to quantify the particles produced in-situ, the photoluminescence from airborne gold, silver, and copper nanoparticles was studied, and spectrally characterized. The quantum efficiency of photoluminescence from gold nanoparticles was determined, providing an optical diagnostic tool for future quantitative in-situ measurements. The second part concerns the metal-organic vapor providing the metal atom that constitute the trunk of the nanowires. An optically accessible reactor setup was constructed. Indium atoms were produced both by pyrolysis and pulsed laser photolysis and studied quantitatively using high resolution laser-induced fluorescence and absorption spectroscopy, spatially and temporally resolved. Scattering measurements revealed large amounts of indium droplets produced by pulsed photolysis.

Key words
Nanoparticles, Nanowires, Aerotaxy, Laser diagnostics, Absorption, Laser-induced fluorescence, Photoluminescence, Spark ablation, Plasma

Classification system and/or index terms (if any)

Supplementary bibliographical information

Language
English

ISSN and key title
1102-8718

ISBN
978-91-7895-853-5 (print)
978-91-7895-854-2 (pdf)

Recipient's notes

Number of pages
137

Price

Security classification

Towards optical diagnostics and control in aerotaxy semiconductor nanowire growth

by Per Samuelsson

LUND
UNIVERSITY

A doctoral thesis at a university in Sweden takes either the form of a single, cohesive research study (monograph) or a summary of research papers (compilation thesis), which the doctoral student has written alone or together with one or several other authors.

In the latter case the thesis consists of two parts. An introductory text puts the research work into context and summarizes the main points of the papers. Then, the research publications themselves are reproduced, together with a description of the individual contributions of the authors. The research papers may either have been already published or are manuscripts at various stages (in press, submitted, or in draft).

Funding information: The thesis work was financially supported by the Knut and Alice Wallenberg Foundation, and the Swedish Energy Agency

Faculty of Engineering, Department of Physics

Lund Reports on Combustion Physics LRCP-231
ISBN: 978-91-7895-853-5 (print)
ISBN: 978-91-7895-854-2 (pdf)
ISRN: LUTFD2/TFCP-231-SE
ISSN: 1102-8718

Printed by Tryckeriet i E-huset, Lund, Sweden, April 2021

Populärvetenskaplig sammanfattning

Det finns idag ett stort behov av att finna förnybara alternativa energikällor för att täcka framtida energibehov. Solen kan förse oss med oerhört stora mängder energi, men solceller är fortfarande relativt ineffektiva och dyra att framställa, och används därför i mindre utsträckning. Genom att effektivisera produktionen, samt använda billigare och material som mer effektivt kan utnyttja solenergin, kan detta bli ett mer attraktivt alternativ. Det övergripande syftet med arbetet bakom avhandlingen är att försöka effektivisera en del i produktionsprocessen, genom att studera, och förstå tillväxten hos nanotrådar, mikroskopiska komponenter som har förutsättningar att öka effektiviteten hos solcellerna. På grund av deras ringa storlek – några tiotal nanometer i diameter gånger ett par mikrometer – i förhållande till ljusets våglängd, ca 450 nm för blått ljus – har nanotrådar av halvledarmaterial förmågan att fånga in en större andel av det inkommande ljuset som omvandlas till elektrisk effekt. Traditionellt sett har nanotrådar producerats genom att låta dem växa från ett platt substrat (epitaxi). Genom att låta tillväxtprocessen istället ske utspritt i en aerosol (aerotaxi), inte helt olikt hur iskristaller bildas i atmosfären, kan tillväxthastigheten effektiviseras dramatiskt. I likhet med iskristaller behövs det en kärna, eller ett frö från vilken resten av tråden eller partikeln kan växa. I atmosfären utgörs kärnan ofta av dammkorn, medan det hos nanotrådarna består av guldpartiklar med en diameter på omkring 50 nm. Resten av tråden (stammen) utgörs av ett halvledarmaterial som består av ämnen tillhörande grupp III och V i periodiska systemet, t.ex. indium, gallium, aluminium, respektive fosfor, arsenik, samt antimon. Inom ramen för avhandlingsarbetet har fokus lagts på dels guldpartiklarna, och dels atomärt indium, samt trimetylindium som är den form i vilken indium ofta levereras. En aerosol av metallpartiklar eller en ånga bestående av fria atomer studeras lämpligen optiskt. Genom att belysa ett föremål, t.ex. en partikel eller en atom, och sedan analysera ljuset som passerar genom föremålet (absorption), eller ljus som absorberas och sedan sänds ut med en annan, ofta längre, våglängd (fluorescens eller fotoluminiscens) kan vi studera dess egenskaper samt, indirekt, dess omgivning. Ljuskällan är ofta en laser, och detektorn kan vara, t.ex., en fotodiod eller CCD-kamera. Allmänna egenskaper som beskriver lasrar som använts i avhandlingsarbetet är t.ex. ett extremt smalt våglängdsintervall (färg), hög ljusintensitet, koherens (alla fotoner har samma fas), samt riktning. På motsvarande sätt kan fria atomers och enkla molekylers spektra (d.v.s. atomer och molekyler i gasfas) karakteriseras av individuella smala absorptionslinjer, på grund av deras höga grad av symmetri. Genom att kombinera en avstämbar laser vars våglängd överensstämmer med en av dessa atomabsorptionslinjer, samt en detektor som enbart ser atomen i fråga (t.ex. med hjälp av ett optiskt filter), erhålls ett analysverktyg, en fluorescensspektrometer, med mycket hög känslighet.

I avhandlingsarbetet har en ånga av indiumatomer studerats genom att belysa dem med violett ljus. Atomerna exciteras till en högre energinivå, för att sedan sända ut blått ljus när de återgår till ursprungstillståndet. Indiumatomerna producerades på två olika sätt, dels

genom pyrolys av trimetylindium, d.v.s. genom uppvärmning, och dels genom fotolys, genom att belysa trimetylindium med en kort ultraviolett ljuspuls, vilket får trimetylindium att sönderfalla och producera fria indiumatomer. Avsikten med detta är att vi dels erhåller en slags kontroll över processen, både i form av ett analysverktyg, men vi kan även använda det för att påskynda en process, t.ex., kristalltillväxt. Genom mätningar kan vi skapa en bild av den kemiska miljö och förutsättningar vad beträffar t.ex. temperatur, koncentration, utbredning och andra egenskaper hos olika ämnen som gör kristalltillväxt möjlig och på så sätt förstå och påverka processen. Detta har genomgående varit själva kärnan i projektet, att samtidigt observera och påverka föremålet för studien med hjälp av ljus, eftersom det ger oss möjlighet att, beröringsfritt, påskynda en kemisk process en önskvärd riktning.

Den andra delen av projektet berör guldpartiklarna som fungerar som katalysatorer för trådstillväxten. För att undvika kontamination vid tillväxtprocessen ställs det höga krav på renhet i tillväxtmiljön, som därför sker i ren kvävgas. Partiklarna produceras genom att låta en metallånga av guldatomer kondensera, och återigen kan vi dra paralleller till hur t.ex. regndroppar bildas i atmosfären från vattenånga. Ångan produceras i detta fall i en periodisk gnisturladdning mellan två guldelektroder i kvävgas. Varje gång en urladdning sker, värms elektrodytorna upp och en liten mängd guld förångas. Dessa guldatomer kan mätas på motsvarande sätt som beskrivits ovan, med hjälp av absorptionsspektroskopi och laser-inducerad fluorescens, med syftet att förstå förutsättningarna för att producera guldpartiklar med önskvärda egenskaper.

I motsats till atomer och molekyler har fasta material i allmänhet breda absorptionsspektra (vissa kristaller utgör ett undantag). En rund guldpartikel med diametern 50 nm består av ungefär fyra miljoner guldatomer, och varje atom stör sina närmaste grannar, vilket medför att deras energinivåer, och därmed smetas deras spektrum ut. Dessa kan dock studeras på liknande sätt som beskrivits ovan genom att analysera ljuset de sänder ut när de belyses med en laser, dock med den väsentliga skillnaden att det utsända ljuset nu består av våglängder som täcker hela det synliga området, samt att det är betydligt svagare.

List of publications

This thesis is based on the following publications, referred to by their Roman numerals:

I **Optical measurements in a spark discharge plasma for gold nanoparticle synthesis**

P. Samuelsson, M. H. Magnusson, K. Deppert, M. Aldén, and Z. S. Li
Manuscript in preparation

II **Airborne gold nanoparticle detection using photoluminescence excited with CW laser**
P. Samuelsson, M. Snellman, M. H. Magnusson, K. Deppert, M. Aldén, and Z. S. Li
Manuscript submitted for publication

III **Optical diagnostics on trimethylindium pyrolysis and photolysis for functional nanoparticle generation**
P. Samuelsson, M. H. Magnusson, K. Deppert, M. Aldén, and Z. S. Li
Manuscript in preparation

Publications not included in this thesis:

Strategy for improved NH_2 detection in combustion environments using an alexandrite laser
C. Brackmann, B. Zhou, **P. Samuelsson**, V. A. Alekseev, A. A. Konnov, Z. S. Li, and M. Aldén
Spectrochim. Acta A 185, 235–242 (2017).

High temperature laser excitation spectrum of indium hydroxide

P. Samuelsson, C. M. Western, M. Aldén, and Z. S. Li
Manuscript in preparation

Contents

Chapter 1

Introduction

Nanowires are tiny (some microns in length, by some tens of nanometers in diameter) semiconductor components, in the present case made up by elements in groups III and V in the periodic table, which includes indium, gallium, aluminum, and phosphor and arsine. In epitaxy the wires are grown from nucleation centers placed on a heated substrate. By introducing the constituent materials using high vapor pressure precursor molecules, which decompose at the growth site, the wires are grown layer by layer at atomic scale using a self-assembly mechanism driven by thermodynamics. By suitable choice of materials, and successive introduction of the precursors during growth, wires can be tailored to act as p–n junctions, ubiquitous components in integrated electronics and fundamental building blocks for solar cells. By decreasing the size of the components, approaching the wavelength of the light that they are designed to collect, they can be made highly efficient, but at the same time, more of them are necessary in order to cover the same surface. Whereas nanowires have the potential to become both more economic regarding material consumption and more efficient as an alternative to conventional components, in order for nanowires to become a commercially viable alternative, techniques are needed for massive production at low cost, with minimal rejection ratio.

The subject of the present thesis is not semiconductor nanowire growth, or laser spectroscopy, but an attempt to bridge the gap between two very different research communities that have developed over decades, in parallel, but more or less isolated from each other. Initial attempts at laser photochemistry and laser diagnostics were pioneered by Osgood et al. [1] and Richter et al., [2] respectively, during the 1980s and early 1990s, however, much has happened since the 1980s in both the semiconductor field and within laser diagnostics; lasers and photonics have seen a tremendous development, particularly with the emergence of new light sources and most notably light-emitting diodes (LEDs), culminating in the 2014 Nobel prize in physics being awarded the inventors of the blue LED, Isamu

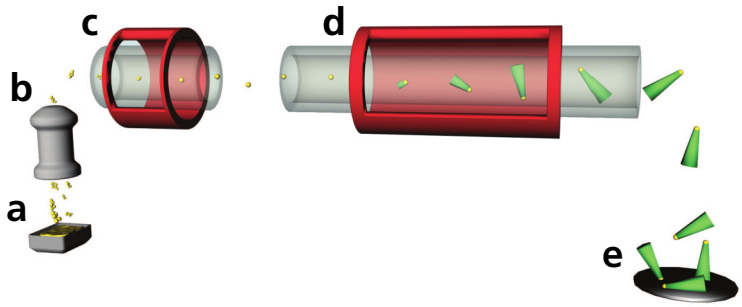

Figure 1.1: Illustration of nanowire growth by aerotaxy: **(a)** Gold is vaporized in a furnace, and condenses into agglomerates. **(b)** The agglomerates carried in a nitrogen flow and are size selected in a differential mobility analyzer (DMA). **(c)** The agglomerates are sintered into spherical gold nanoparticles in a compaction furnace. **(d)** Metal-organic precursors are mixed with the gold nanoparticle stream in a growth furnace, and wires are grown continuously in gas phase. **(e)** The wires are collected. Originally published in Ref. [4].

Akasaki, Hiroshi Amano, and Shuji Nakamura. Fittingly, the development of particularly blue LEDs has been one of the driving forces within the semiconductor industry, pushing emission wavelengths to shorter wavelengths and eventually to the ultraviolet, leading to the initiation of the project resulting in this thesis.

One of the most promising developments in the last decade has been the invention of semiconductor nanowires grown directly in gas-phase (aerotaxy) instead of using a fixed substrate. [3, 4] The wires are then grown continuously, catalyzed by metal nanoparticles distributed in an aerosol, as illustrated in figure 1.1. In the illustration, gas-borne gold nanoparticles are produced by vaporization of gold in a furnace and subsequent condensation into agglomerates. The gold agglomerates are size-selected, and then passed through a furnace causing them to sinter into spherical particles, now with a narrow size distribution. The gold nanoparticles are mixed with metal-organic precursors inside a second furnace or reactor, and the wires continuously grow from individual nanoparticles in the gas phase. Elimination of the conventional substrate removes the main obstacle to efficient growth, which is the transport limitation imposed by the substrate. As a result, nanowires grown by aerotaxy have a dramatically increased growth rate compared to epitaxial (surface-based) growth. Highly relevant to the current work is the fact that elimination of the substrate enables use of optical tools to monitor and influence growth without interference, allowing the use of higher powered lasers required for detection of trace species, and optical manipulation through photochemistry.

Conventionally, analysis of the wires produced is done in batch, i.e., the particles are grown in one lab, and then transported to another lab and analyzed using scanning electron microscopy (SEM), tunneling electron microscopy (TEM), x-ray diffraction (XRD), and other techniques which have the ability to analyze the detailed structure including individ-

ual atoms on an elemental basis. Whereas it is not possible to resolve the nm-size structures using light at optical wavelengths, it offers in some ways an even sharper tool in high resolution laser spectroscopy, which allows us to image the distribution of an ensemble of atomic and molecular species orders of magnitudes smaller, as well as their concentration and temperature distribution with high specificity thanks to their individual spectral imprints. More importantly, this can be done under operando conditions, i.e., we can observe the growth live, and image the necessary growth parameters in-situ, and due to the continuous growth, it allows us to continuously tune the process using feedback.

The necessity for imaging of the growth volume led to the design of an optically accessible reactor, which captures the most important aspects of the aerotaxy growth environment, viz. absence of oxygen and other contaminants, and with the ability to tune the temperature over the required range. The fact that aerotaxy takes place at atmospheric pressure means that the vacuum chamber can be eliminated. The reactor was therefore designed as an open-ended system with unrestricted optical access with respect to scattering, transmittance and polarization, resulting in a high level of flexibility, but it also means that highly toxic precursors such as arsine and phosphine must be avoided. On the brighter side this promotes development towards greener alternatives like GaN grown by trimethylgallium and ammonia.

In the work of this thesis, gas-borne gold nanoparticles were produced in a spark discharge. In order to work as catalysis for nanowire growth, incorporation of contaminants or oxidation must be avoided, and spark discharge generation results in particles largely free from contaminants which is inherent in various chemical processes as well as in flame synthesis. The spark discharge aerosol generator consists of a high voltage supply or capacitor charger, a capacitor bank, and a discharge cell. Mounted inside the cell are two gold electrodes, one grounded and the other connected to the capacitor bank. By continuously charging the capacitor bank, it will periodically discharge across the electrodes, resulting in heating of the electrode surfaces. During each spark, a small amount of gold is ablated, which condenses into particles, and led away using a nitrogen flow. The spark discharge generation process results in a high degree of flexibility and tunability, and the high-temperature plasma formed between the electrodes is a highly complex process.

1 Outline of the thesis

The rest of this thesis is structured as follows:

In chapter 2 the spark discharge generator for generating gas-borne gold nanoparticles is described. The discharge plasma and specifically the plume of gold atoms ablated from the electrodes were studied using emission spectroscopy, laser absorption spec-

troscopy, and two-photon laser-induced fluorescence, with the aim to describe the distribution and concentration of ablated gold. The discharge system was characterized electrically, and the size distribution and number density of particles generated were determined.

In chapter 3 gold nanoparticles in a nitrogen flow were investigated optically using photoluminescence, excited using a continuous wave laser, detected using a spectrometer, and imaged using a camera. Laser heating and thermal emission of plasmonic nanoparticles is discussed.

In chapter 4 an open-air aerotaxy reactor is described, and the pyrolysis and photolysis of trimethylindium was investigated. Free indium atoms generated by pyrolysis or pulsed ultraviolet laser photolysis of trimethylindium was studied using high resolution laser spectroscopy and laser-induced fluorescence, enabling quantitative imaging of the indium in the reactor.

In chapter 5 results from preliminary measurements on the gas-phase gold-indium alloying process is presented, which is the first step in the nanowire growth process. The increase in indium in the gold nanoparticles at high temperatures was investigated using a combination of pulsed laser ablation and laser-induced fluorescence of indium atoms.

Chapter 6 is a summary of the contents of the thesis, and advice or suggestions for continued investigation is discussed.

Chapter 2

Metal nanoparticle generation by spark ablation

Spark ablation or spark discharge generation is one of the most promising ways of generating metal nanoparticles in the gas phase. [5] Compared to, e.g., flame synthesis it is clean, both in the sense that contaminants incorporated in the nanoparticles, such as oxygen or carbon, are kept to a minimum, but also that no waste is produced if the particles are generated in inert gas, e.g., nitrogen. An important advantage is the flexibility that nanoparticles of almost any material can be generated by choice of electrode material. Catalytic seed particles are commonly produced from precious materials, e.g., noble metals like gold and platinum, however, post processing of the particles is usually necessary in order to turn the particles generated into monocrystalline, spherical particles with a specific, narrow size distribution. With better understanding and control of the particle generation process, less processing may be needed, resulting in less wasted material. Finally, spark ablation is scalable to industrial level production. Physical parameters such as breakdown voltage, i.e., properties of the carrier gas, capacitance, inductance and resistance of the discharge circuit, as well as electrode geometry, and properties of the electrode material—all contribute to the properties of the generated particles, resulting in a highly complex process. Intelligent choice of design parameters, enabled by better understanding of the generation process, through on-line optical measurements, may guide development toward more efficient generators with reduced power consumption and amount of electrode material. In this work both emission, and laser-diagnostic techniques were used for studying the discharge for generation of gold nanoparticles. The aims of these measurements was to measure and visualize the gold ablated from the electrodes during a discharge using non-intrusive optical techniques, but in order to do so it is necessary to have the pre-knowledge about the environment, i.e., the spark discharge plasma, with regard to temperature and composition.

The results were reported in Paper I.

The chapter is outlined as follows: In section 1 the experimental setup and the particle generation process are described. Results from electrical measurements on the discharge is presented, and the amount of gold ablated per spark is estimated from the energy dissipated in the spark. In section 2 emission spectroscopy is used for determining the temperature of the plasma plume. In section 3 two-photon laser-induced fluorescence and laser absorption spectroscopy are applied to the discharge, for spatially and temporally mapping the distribution of the gold atom plume ablated from the electrodes. Synchronization between the spark discharge and a pulsed laser is discussed. Finally, in section 4 the particles generated by the discharge system are characterized using a scanning mobility particle sizer (SMPS).

1 Experimental setup and operation

Shown in figure 2.1 is a system overview of the spark discharge aerosol generator used in the measurements presented here, and in Paper I. A constant-current high voltage supply or capacitor charger (CCR) continuously charges a capacitor bank. The two electrodes of the chosen material are mounted inside a discharge chamber, with one electrode connected to the positive polarity of the capacitor bank, and the other electrode connected to the chamber and grounded. The CCR will keep charging the capacitor bank at a set charging current until the voltage setpoint is reached, or until breakdown occurs between the electrodes, at which point an arc is formed, acting as a conductive channel across the spark gap. By closing the circuit, the capacitor bank is discharged, and the process is repeated.

The general evolution of a spark discharge is illustrated below:

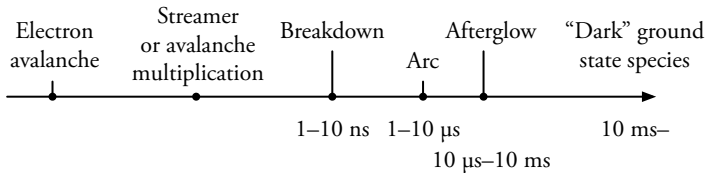

Breakdown of the carrier gas due to a strong electric field over the electrodes triggers an electron avalanche, which grows into a streamer or Townsend avalanche, [6] forming a conducting channel between the electrodes. At this point current starts to rush across the channel, resistively heating the carrier gas and electrode spots, forming what is usually referred to as an arc, as shown in the top right of figure 2.1. In the case of the specific discharge studied here, the resistance, inductance and capacitance of the discharge circuit cause a damped oscillation in the voltage and current during the arc stage, resulting in a modulation of the power deposited into the discharge channel and the electrodes over several microseconds after breakdown. [7] This has the consequence that the polarity is periodically reversed over the electrodes during discharge, and the electrodes alternate between being the momentary

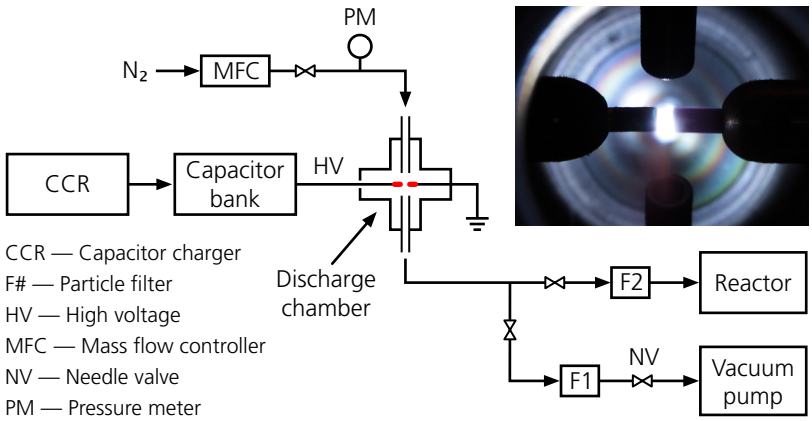

Figure 2.1: System overview of the spark discharge generator. Depending on the experiment, the particles may be directed either to the reactor described in chapter 4, or filtered. The particle filter F1 removes virtually all particles from the flow, whereas F2 removes particles larger than 0.8 µm. The electrodes are indicated in red in the diagram. Shown to the upper right is a photograph of the spark discharge, where the horizontal gold electrodes are seen on either side of the bright spark.

cathode and anode. In the afterglow the current has ceased, but the plasma is still hot and emitting. In the wake of this is a final step that is usually neglected, which is the remaining cloud of atomic species in the ground state, which have yet to recombine. The plasma here is not as bright, so less observations have been reported, but still measurable using absorption spectroscopy and laser-induced fluorescence.

1.1 Electrical measurements of current and voltage waveforms

It can be expected that the periodic voltage reversal discussed earlier will have a large influence on both how the electrodes are ablated, and the characteristics of the resulting plasma. The temperature of the plasma would determine, e.g., what atomic and molecular species, and their ions, can be expected. In order to characterize the discharge electrically with respect to the instantaneous power deposited in the discharge channel, the voltage and current over the electrodes were measured as a function of time after breakdown. By integrating the dissipated power, the spark energy deposited into the discharge channel and electrodes is obtained, which can be related to the amount of ablated gold.

Shown in figure 2.2 is an electrical diagram of the spark discharge generator. The voltage and current were measured using a voltage probe (P6015A, Tektronix) and a current probe respectively (Model 110, Pearson). Both probes were located inside the shielded aluminum box, at the points indicated in figure 2.2. The voltage probe has an attenuation factor 1 000, whereas the current probe outputs $0.1\,\mathrm{V\,A^{-1}}$, requiring additional attenuation, due

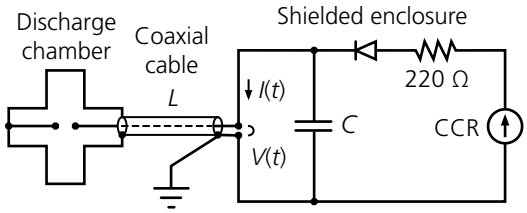

Figure 2.2: Electrical circuit diagram of the spark discharge generator. $V(t)$ and $I(t)$ indicates the locations of the voltage and current probes, respectively. The chosen capacitor bank capacitance is C, and the discharge chamber is connected to the capacitor bank using a coaxial cable, which introduces an inductance L. The total resistance of the discharge circuit is R (not depicted).

to the high peak current. The oscilloscope was usually triggered by the rapid increase in the current as the energy stored in the capacitor bank is discharged across the spark gap shortly after breakdown, which is sufficiently accurate at the time scales considered. The parameters of the discharge circuit are summarized in table 2.1.

The spark gap distance can be varied by moving the grounded electrode, which is mounted on a linear motion vacuum feed-through. The spark gap, together with the carrier gas and pressure, determines the breakdown voltage, and therefore the discharge energy. Ten voltage and current waveforms were collected at each spark gap, the parameters of the waveforms were fitted for each individual single shot measurement, and the resulting parameters averaged. An example waveform is shown in figure 2.3, and the results from the measurements are summarized in table 2.3. The specified uncertainties (within parentheses) reflect the spread of the fitted parameter values at each spark gap, and do not account for the uncertainty in, e.g., the spark gap distance itself, or instrumental accuracy. Moreover, it should be noted that the discharge conditions are sensitive to the electrode geometry, surface roughness, and other factors which vary over time.

Table 2.1: Summary of physical quantities and their typical values, for generation of gold nanoparticles in nitrogen at ambient pressure

d	0.5 to 3 mm	Distance between the two facing electrode surfaces
C	20 nF	Total capacitance of the capacitor bank
I_{set}	5 to 10 mA	CCR charging current setpoint
I_{charge}	$I_{\mathrm{charge}} \leq I_{\mathrm{set}}$	Actual charging current, typically smaller than I_{set}
V_{set}	12 kV	CCR voltage setpoint for free-running discharge
V_{b}		Breakdown voltage, i.e., voltage over the electrodes the moment before breakdown
$V(t), I(t)$		Measured voltage and current as a function of time after breakdown ($t = 0$), as indicated in figure 2.2
W_{spark}	$\frac{1}{2}CV_{\mathrm{b}}^2$	Maximum energy stored in the capacitor bank
f_{spark}	$I_{\mathrm{charge}}(CV_{\mathrm{b}})^{-1}$	Spark repetition rate (SRR)
	1.5 L min^{-1}	Carrier gas flow rate

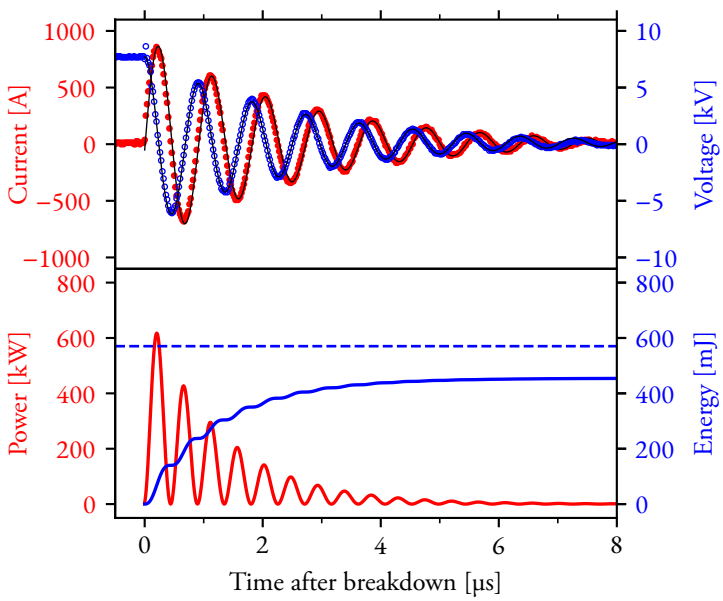

Figure 2.3: **Upper panel:** Example waveform at 2 mm spark gap in nitrogen and 12 kV voltage setpoint, and 5 mA current setpoint. The blue (open circles) and red (filled circles) curves are the experimentally obtained voltage and current waveforms, and the solid black curves are the respective fits. **Lower panel:** The instantaneous power calculated from the fitted current waveform, and the cumulatively integrated power, i.e., the discharge energy. The dashed blue curve is the discharge energy estimated using equation (2.5).

Calculation of discharge energy and amount of ablated gold

In this section the calculation of the estimated amount of gold ablated from the electrodes will be outlined. The electrode erosion mechanism is generally understood as thermal evaporation of the electrode material, where hot spots on the electrode surfaces are heated to the boiling point, by joule heating and impact heating. The mass of the ablated material is found from energy balance at the electrodes, where the spark energy is the source, and the most important sink is the thermal conductivity of the electrode material, [8, 7] as discussed below. The energy deposited into the discharge (spark energy) is found by integrating the dissipated power.

From energy balance at the electrode surfaces, we have the following approximate expression for the mass m evaporated from the electrodes per spark: [8]

$$m = \frac{W_{\text{spark}} - Q - H}{E_{\text{vap}}}, \tag{2.1}$$

where W_{spark} is the spark energy, Q the energy lost as Planck radiation, H the heat dissipated by conduction through the electrodes, and E_{vap} the energy per unit mass required for heating, melting and evaporating the electrode material. The thermal conductivity of the gas medium is neglected in this model. The individual contributions are given by

$$Q = A\varepsilon\sigma T_{\text{b}}^4 \Delta t, \qquad \text{Planck radiation} \tag{2.2}$$

$$H = 2\sqrt{\pi A}(T_{\text{b}} - T)k\Delta t, \qquad \text{Heat conduction} \tag{2.3}$$

$$E_{\text{vap}} = c_p^s(T_{\text{m}} - T) + \Delta_{\text{fus}}H + c_p^\ell(T_{\text{b}} - T_{\text{m}}) + \Delta_{\text{vap}}H, \qquad \text{Evaporation} \tag{2.4}$$

where Δt is the spark duration, taken as the time constant of the amplitude decay of the current waveform, A the hot spot area, with a radius in the order of a few micrometers, [7] and ε the emissivity of the electrodes, assumed to be $\varepsilon = 1$, and $\sigma = 5.67 \times 10^{-8}\ \text{W m}^{-2}\ \text{K}^{-4}$ (Stefan–Boltzmann constant). The rest of the parameters are listed in in table 2.2.

The discharge energy W can be estimated by the the energy stored in the capacitor bank,

$$W_{\text{spark}} = \tfrac{1}{2}CV_{\text{b}}^2, \tag{2.5}$$

where V_{b} is the breakdown voltage, and C the effective capacitance. The expression for W_{spark} in equation (2.5) is the energy stored in the capacitor, however the true energy deposited into the discharge channel and the electrodes will be somewhat lower. In order to obtain a better estimate, we instead integrate the instantaneous power dissipated at the electrodes. By fitting an expression of the following form to the current waveform:

$$I(t) = I_0 e^{-t/\tau}\cos(\omega t + \varphi), \quad t \geq 0, \tag{2.6}$$

Table 2.2: Physical properties of gold

T	Initial temperature	300 K
T_m	Melting temperature	1 337 K
T_b	Boiling temperature	3 109 K
k	Thermal conductivity	0.025 W m^{-1} K^{-1}
c_p^s	Specific heat capacity[a](solid)	140 J kg^{-1} K^{-1}
c_p^ℓ	Specific heat capacity[b](liquid)	167 J kg^{-1} K^{-1}
$\Delta_{fus}H$	Enthalpy of melting	6.46×10^4 J kg^{-1}
$\Delta_{vap}H$	Enthalpy of vaporization	1.87×10^6 J kg^{-1}

[a] T = 800 K [9]
[b] T = 1 337 K

the resistance R and inductance L can then be obtained from the relations [10]

$$\tau = \frac{2L}{R}, \qquad \omega = \sqrt{\frac{1}{LC} - \frac{R^2}{4L^2}}. \tag{2.7}$$

To obtain an estimate of the energy W_{spark} deposited, we can now integrate the instantaneous power $P(t) = U(t)I(t)$ over the entire duration of the waveform. Because this requires that the phase between the voltage and current waveforms is accurately known [10] we instead integrate $\tilde{P}(t) = R\tilde{I}^2(t)$, where $\tilde{I}(t)$ is the fit to the current waveform and R the resistance obtained from equation (2.7), so that

$$\widetilde{W}_{spark} = R \int_0^\infty \tilde{I}^2(t)\, dt. \tag{2.8}$$

With typical values, the calculated evaporated mass m is in the order of 10 to 100 ng per spark.

Table 2.3: Result of electrical measurements at 12 kV and 5 mA voltage and current setpoints. Note that V_0 and I_0 represent the respective waveform amplitudes.

Case	d mm	f_{spark} Hz	V_0 kV	I_0 A	τ µs	R Ω	L µH	$\widetilde{W}_{\text{spark}}$ mJ
(a)	0.74	40	4.63(6)	623(10)	2.40(3)	0.965(5)	1.16(1)	225(10)
(b)	0.93	37	5.12(7)	678(5)	2.43(2)	0.921(11)	1.12(1)	259(5)
(c)	1.37	33	6.10(12)	778(8)	2.48(1)	0.875(9)	1.08(1)	332(7)
(d)	1.58	32	6.93(9)	865(11)	2.52(2)	0.845(10)	1.06(1)	403(10)
(e)	2.01	29	7.58(10)	933(13)	2.51(2)	0.816(10)	1.03(1)	452(13)
(f)	2.21	29	8.10(5)	980(12)	2.49(2)	0.817(11)	1.02(1)	495(13)
(g)	2.64	26	9.04(13)	1063(25)	2.53(2)	0.775(11)	0.98(1)	567(24)

2 Plasma characterization using emission spectroscopy

Emission spectroscopy is a well-established optical technique for plasma diagnostics. Depending on the density of the spectrum and the instrumental resolution, several atomic and molecular species may be measured simultaneously, resulting in good statistics. As a starting point for a high-resolution spectroscopic investigation of a pulsed discharge, it helps to establish an overview of which species can be expected, at a given point in time. Shown in figure 2.4 is a spectrogram constructed by combining emission spectra of a Au–N_2 spark discharge collected at increasing time delay after breakdown. Also shown in figure 2.4 is the time-resolved intensity integrated over the displayed wavelength interval, compared to the instantaneous power deposited into the discharge channel, which was calculated in the previous section. During the first voltage reversal cycle, up to approximately 0.5 µs after breakdown, the emission consists of almost entirely of broadened emission lines belonging to various ionization levels of the carrier gas, as well as a broad continuum.

High resolution spectra collected 275 ns after breakdown are dominated by N III emission, as well as N II and N IV. Analysis of the lineshape of the 399.5 nm N II emission line, (not depicted) which is relatively free of interference, indicates a Lorentzian linewidth of approximately 0.5 nm, which had narrowed to the instrumental linewidth 0.1 nm by 2 to 4 µs, making it a good candidate for estimating the electron density in this interval. [11]

Emission from the electrode material reaches maximum only after several microseconds, and as the plasma cools down, progressively lower ionization levels can be observed in emission. Strong emission from singly ionized gold (Au II) around 220 nm reaches maximum emission intensity at approximately 2 µs, and emission from neutral gold (Au I) at 243 nm and 268 nm approximately 4 µs after breakdown. From high resolution spectra covering 190 to 320 nm (not depicted), collected 2.4 µs after breakdown, 75 lines could be identified belonging to Au II, and six to Au I, including the 201 nm emission line. Some lines are indicated at the top of figure 2.4.

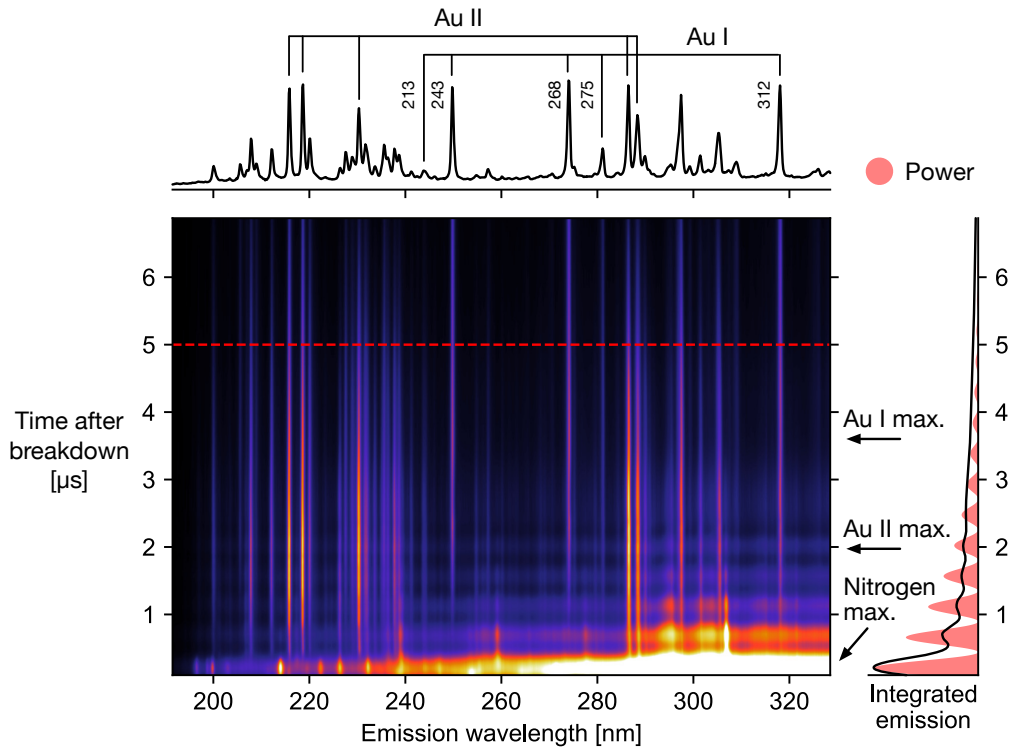

Figure 2.4: Low resolution spectrogram showing the spectrally and temporally resolved ultraviolet emission of an Au–N_2 spark at ambient conditions. Shown in the upper panel is the instantaneous spectrum at 5 µs after breakdown. The wavelength of some of the stronger emission lines of Au I and Au II are indicated. Shown in the right panel is the spectrally integrated and temporally resolved ultraviolet emission intensity (solid black curve), which follows the instantaneous power waveform. Also shown as comparison is the power waveform (filled red curve), obtained from measurements of the discharge current.

During the first few microseconds an intensity modulation is observed in the continuum emission and in some emission lines. The emission intensity modulation reflects the instantaneous deposited power, shown in figure 2.3, where it can also be seen that until about 4 µs energy is still being deposited into the discharge channel, resulting in heating of the carrier gas and the gold atoms. The fact that the intensity modulation mostly appears to affect the carrier gas species suggests that thermal excitation of atoms and ions belonging to the electrode material is a secondary process.

Temperature estimation and spectral fitting

In Paper I emission spectroscopy was used to determine the temperature of the plasma at around 5 µs after breakdown, by fitting the emission spectrum of several Au and In lines. Using two different electrode materials, the number of analytic lines available for analysis was increased at longer delays after breakdown.

The general model and the approach to the fitting procedure will now be outlined. In short, an emission spectrum is calculated based on information extracted from the NIST atomic spectra database (ASD), [12] which is compared to the intensity of selected lines in the observed spectrum. It is assumed that the plasma is at local thermodynamic equilibrium (LTE), i.e., that at any given point in space and time, the degree of ionization is given by the Saha equation (ionization equilibrium), [13] and the population of atomic and ionic energy levels are given by the Boltzmann distribution. It is furthermore assumed that the plasma is quasi-neutral, i.e., the total charge of all electrons and ions equals zero (charge neutrality), and that the plasma acts as an ideal gas, where the sum of the partial pressures of all neutral atoms, ions, and electrons is a constant total pressure $p = 1\,\mathrm{bar}$ (constant pressure). These assumptions may hold to different degrees during the evolution of the plasma, and to what extent they hold will be determined from the quality of the fit. The result is an equation system:

$$\begin{cases} p/kT = n_\mathrm{e} + n_0 + n_1 + n_2 + \cdots & \text{Constant pressure} \quad (2.9a) \\ 0 = -n_\mathrm{e} + n_1 + 2n_2 + \cdots & \text{Charge neutrality} \quad (2.9b) \\ \dfrac{n_\mathrm{e} n_1}{n_0} = \dfrac{2(2\pi m_\mathrm{e} kT)^{3/2}}{h^3} \dfrac{Q_1(T)}{Q_0(T)} \exp\left(-\dfrac{\chi_0}{kT}\right) & \text{Ionization equilibrium} \quad (2.9c) \\ \vdots \\ \dfrac{n_\mathrm{e} n_z}{n_{z-1}} = \cdots \end{cases}$$

where n_e is the electron density, and $n_0, n_1, n_2, \ldots, n_z$, the respective number densities of neutral, singly and doubly ionized atoms, and so on, and χ_i their ionization energies. The maximum ionization level z is chosen based on temperature. Here $z = 0$ indicates the neutral atom, $z = 1$ the atom with one electron removed, and so on. The parameter m_e is the electron mass, k the Boltzmann constant, and h the Planck constant. The unknown parameters are the number densities n_i.

The electron, ion, and atom number densities n_i were obtained by solving the system for a given temperature T, which are used as input parameters to the second part of the program, which calculates the emission spectrum. The process outlined in the following section. The simulated spectrum is then compared to the experimental spectrum, and the process is repeated with different input temperatures T until a sufficiently good fit is obtained, or when it is determined that no solution exists.

Calculation of line spectrum

For comparison to the recorded emission spectra, simulations of atomic emission line spectra collected at different times after breakdown were performed, using atomic levels and transition probabilities from Ref. [12]. An example of data is shown in table 2.4. Emission spectra were calculated assuming a Boltzmann distributed population of levels, and weighted by the number densities of each respective ionization level of a particular element, as discussed in the previous section. The line-integrated atomic/ionic emission intensities I_{ki} were calculated (up to a proportionality factor) as

$$\int I_{ki}(\nu)\, d\nu = h\nu_0 A_{ki} \frac{1}{Q} g_k \exp\Big(-\frac{E_k}{kT}\Big), \tag{2.10}$$

where h is Planck's constant, ν_0 the transition frequency, A_{ki} the rate constant for spontaneous emission from level k to i, g_i the multiplicity of level i, and subscripts k and i represents the upper, and lower energy levels of the transition, respectively. The last factor in equation (2.10) is the relative population (Boltzmann fraction) of each level j, i.e.,

$$\frac{n_j}{n} = \frac{1}{Q} g_j \exp\Big(-\frac{E_j}{kT}\Big), \tag{2.11}$$

and summation over all levels gives the partition function $Q = Q(T)$ for each ion,

$$Q = \sum_j g_j \exp\Big(-\frac{E_j}{kT}\Big), \tag{2.12}$$

which was calculated from the levels j available in Ref. [12]. For a simulation involving multiple ions of the same element, the emission intensity is weighted by the mole fraction of each ionization level. The spectrum of one ion is then given by

$$I(\nu) = n \sum g(\nu - \nu_0) \int I_{ki}(\nu)\, d\nu, \quad \int g(\nu)\, d\nu = 1, \tag{2.13}$$

where n is the number density of the emitting ion, and $g(\nu)$ the lineshape function, usually taken as a Voigt function to a first approximation, i.e., a convolution of a Gaussian and a Lorentzian function. In the present case the Gaussian contribution would be mostly be an approximation of the instrumental transfer function, whereas the Lorentzian contribution to the lineshape, during the oscillatory stage of the discharge up to about 1 to 2 µs after breakdown, would be dominated by Stark broadening.

Shown in figure 2.5 is an emission spectrum of a spark discharge, with one gold and one indium electrode. The temperature obtained from the fit (approximately 15 000 K) is within the expected range, and similar to the temperature experienced in an argon plasma. [14]

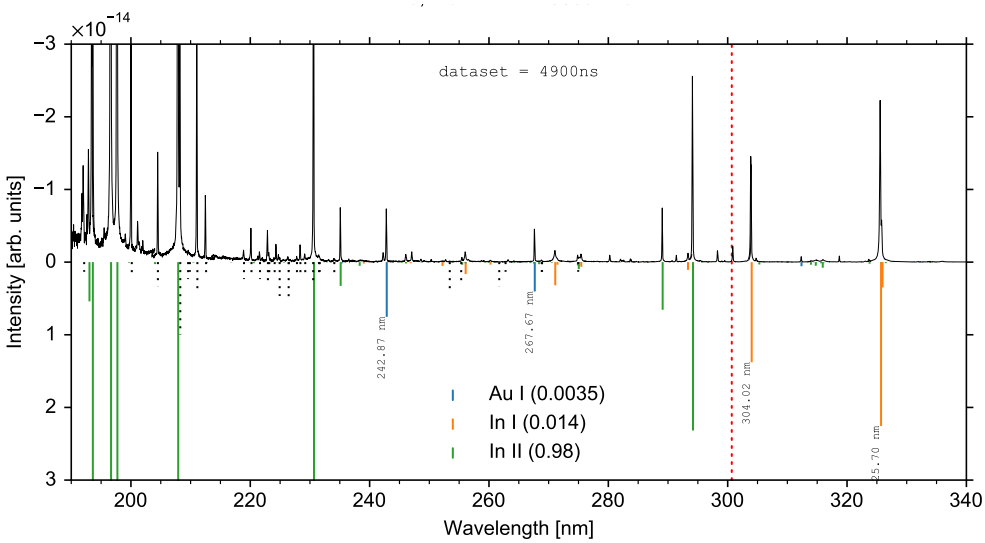

Figure 2.5: Emission spectrum (above) and fitted intensities (below) for chosen Au and In emission lines at 4.9 µs after breakdown. Only the solid lines were included in the fit. The relative abundances of each ion is specified within parentheses. The fit indicates a temperature of approximately 15 000 K.

It was assumed above that the plasma is at LTE. A standard method to determine the existence of LTE is using the Griem criterion, [15] which specifies the minimum electron density required to maintain local thermodynamic equilibrium. The electron density can in turn be determined from lineshape analysis, [11] or by Thomson scattering. [16]

3 Temporally and spatially resolved laser diagnostics

To obtain quantitative diagnostic information about the ablated gold vapor, one must take into account, among other things, the energy structure of the gold atom, interference from other species, as well as measurement geometry and available equipment. In addition to the high spectral resolution required when dealing with a dense spectrum, the inhomogeneity and expansion of the gold vapor plume, and the evolution of the temperature and composition of the spark discharge plasma demands both spatially and temporally resolved measurements, generally only attainable using lasers.

Gold has one stable isotope, ^{179}Au, with nuclear spin $I = 3/2$. There are three allowed transitions from the ground state in the deep UV at 213, 243 and 268 nm; some additional lines are listed in table 2.4. Shown in figure 2.6 is a partial energy level diagram for neutral gold, where some potential excitation schemes for laser-induced fluorescence and absorption of gold atoms have been indicated.

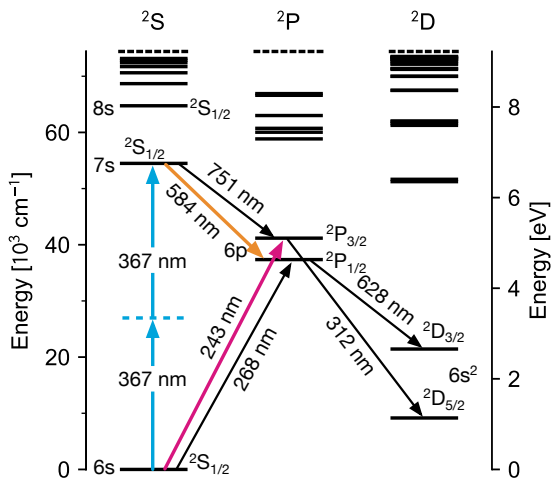

Figure 2.6: Partial energy level diagram of the neutral gold atom (Au I) and relevant transitions for LIF and absorption measurements. The ground state is 6s ^{2}S$_{1/2}$.

Table 2.4: Wavelengths of some relevant Au I lines from the NIST atomic spectra database, [12] and the upper and lower levels of the transitions. The transition rate for spontaneous emission is labeled A_{ki}. Only lines with known transition rates in the NIST database are included in the table.

Wavelength (nm)	A_{ki} (10^8 s^{-1})	Lower level (i)	Upper level (k)
212.7	0.038	$5d^{10}6s\ ^2S_{1/2}$	$5d^9_{5/2}6s_{1/2}6p_{3/2}\ ^4P^o_{3/2}$
242.9	1.980	$5d^{10}6s\ ^2S_{1/2}$	$5d^{10}6p\ ^2P^o_{3/2}$
267.7	1.640	$5d^{10}6s\ ^2S_{1/2}$	$5d^{10}6p\ ^2P^o_{1/2}$
274.9	0.103	$5d^96s^2\ ^2D_{5/2}$	$5d^9_{5/2}6s_{1/2}6p_{1/2}\ ^4F^o_{7/2}$
312.4	0.190	$5d^96s^2\ ^2D_{5/2}$	$5d^{10}6p\ ^2P^o_{3/2}$
583.9	0.295	$5d^{10}6p\ ^2P^o_{1/2}$	$5d^{10}7s\ ^2S_{1/2}$
628.0	0.034	$5d^96s^2\ ^2D_{3/2}$	$5d^{10}6p\ ^2P^o_{1/2}$
751.3	0.424	$5d^{10}6p\ ^2P^o_{3/2}$	$5d^{10}7s\ ^2S_{1/2}$

3.1 Absorption measurements

If the absorption cross section of a given atomic transition, and the abundance of neutral gold relative to ionized gold is known accurately, the concentration along the line of sight can be calculated using Beer's law,

$$T = \exp(-n\sigma\ell), \tag{2.14}$$

where T is the transmittance, spectrally integrated over the absorption lineshape, n the number density of gold atoms, σ the cross section of the absorption line at some given temperature, and ℓ, the absorption path length. Here, σ is a function of excitation frequency. Absorption spectroscopy can advantageously be combined with laser-induced fluorescence (LIF); the LIF observed perpendicularly to the beam can be used to estimate the absorption path length, and the quantitative information yielded by absorption spectroscopy can be used to calibrate the LIF signal. In paper Paper I, ultraviolet CW absorption spectroscopy was used for measuring the transient absorption of neutral gold in the vapor plume formed during a discharge.

The 243 nm absorption beam, corresponding to the $6p\ ^2P_{3/2} \leftarrow\ ^2S_{1/2}$ transition of gold, as shown in figure 2.6, was generated by a CW Ti:Sapphire laser, which will be described in chapter 4. The beam was focused in the center of the spark gap, and the absorption signal was detected using a GaP photodiode, connected to an oscilloscope, which was triggered on the positive flank of the discharge current. The laser wavelength was stepped across the 243 nm absorption line, and the transient absorption signal at each wavelength step was acquired, averaged and normalized, resulting in a two-dimensional map, with excitation wavelength or frequency on one axis, and time after breakdown on the other.

Shown in figure 2.7 is the obtained frequency-resolved transient absorption signal of neutral

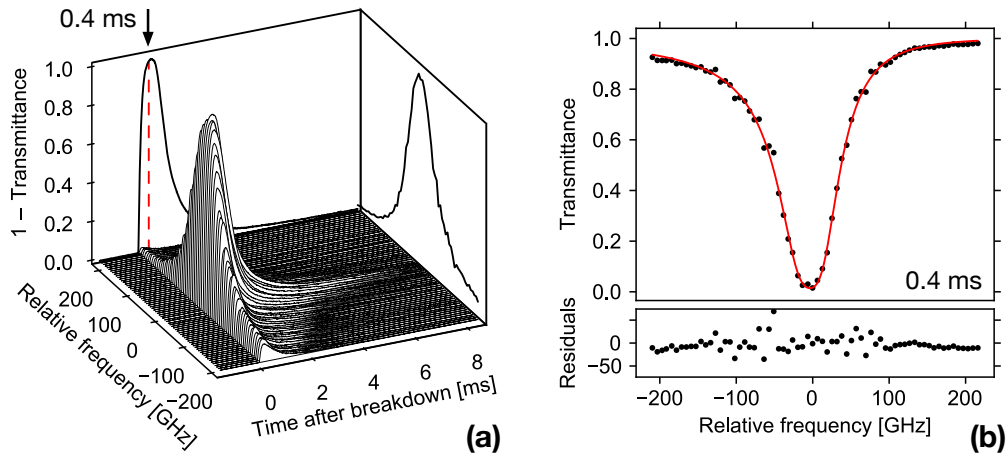

Figure 2.7: Transient absorption of gold atoms in the spark discharge at 243 nm, using the fourth harmonic of the CW Ti:Sapphire laser. The frequency is relative to the center of the 243 nm absorption line. The spark gap was 1 mm. **(a)** Frequency-resolved transient absorption signal. **(b)** Absorption lineshape at 0.4 ms after breakdown. The red solid curve is a fit, using an asymmetric pseudo-Lorentzian lineshape function. [17] The residuals have been magnified by a factor 20.

gold atoms, using 2 mm spark gap. Each individual trace is an average of 100 sparks. The resulting 243 nm absorption lineshapes are in the order of 100 GHz wide (FWHM) and asymmetrical, and the signal approaches optically thick conditions, i.e., the transmittance approaches 100 %. Unlike the gold emission signal shown in figure 2.4, which peaks approximately 4 µs after breakdown, the absorption signal reaches maximum at approximately 400 µs. Combined with a large variance between different sparks, and the associated averaging, the amount of quantitative information that can be obtained from analysis at the peak around 0.4 ms is limited. The opacity could be avoided by instead measuring a weaker resonance transition, e.g., $5d^9_{5/2}6s_{1/2}6p_{3/2}\ {}^4P^o_{3/2} \leftarrow 5d^{10}6s\ {}^2S_{1/2}$ at 213 nm (cf. table 2.4), at the cost of increasing the detection limit.

3.2 Laser ignition of the spark discharge for precise triggering

Due to the strong background, CW lasers are a less attractive option for in-situ imaging of the spark discharge plasma using laser-induced fluorescence, and generally a pulsed probe laser combined with a fast gated camera is required in order to obtain sufficient signal-to-noise to overcome the broadband background emission from interfering lines. The ability to synchronize a pulsed probe laser to the spark discharge is thereby crucial for any measurements on the discharge at a known phase during the discharge waveform.

In order to synchronize a pulsed laser operating at a fixed frequency to a free-running dis-

charge, a separate Nd:YAG laser acting as trigger laser was employed in Paper I. The pulsed trigger laser (532 nm, Brilliant B, Quantel) was synchronized with the probe laser, and by focusing the beam on one of the gold electrodes, typically the initial cathode, a small plasma is generated, which triggers each spark. Using a low trigger pulse energy (approximately 100 µJ) ensures that the characteristics of the plasma are preserved. For laser-triggered operation under conditions comparable to a free-running spark discharge, the voltage setpoint V_{set} was lowered to what the breakdown threshold V_{b} would be for free-running operation (3 to 5 kV typical), and the electrodes moved apart slightly. The spark repetition rate is then determined by the trigger laser, which was 10 Hz in our case, whereas under similar free-running conditions the frequency would be a few tens of Hz.

Laser-triggering of electrical switches is discussed in more detailed in Refs. [18, 19, 20]

3.3 Two-photon laser-induced fluorescence

Laser-induced fluorescence (LIF) provides a powerful tool for studying the ablated electrode material, both spatially and temporally. This could be beneficial, e.g., in mixed particle synthesis, [21] where each electrode consist of different materials. The overlap of the two vapor clouds originating from each electrode would then be crucial in order to generate mixed primary particles.

Using LIF, the most straightforward excitation scheme for gold atoms is excitation from the 6s ground state to the 6p $^2\mathrm{P}_{1/2}$ level at 243 nm, combined with non-resonant detection of the fluorescence at 312 nm, thereby avoiding the elastically scattered laser light, as shown in figure 2.6. The strongest fluorescence is emitted in a spectral region where there is strong background emission from the plasma, as shown in figure 2.4. In an effort to avoid this the feasibility of an alternative detection scheme based on two-photon LIF was evaluated, wherein the fluorescence is instead detected in the yellow or red parts of the spectrum, where there are relatively fewer interfering emission lines.

Using two-photon absorption one can reach otherwise unreachable transitions, e.g., in the deep ultraviolet, at wavelengths otherwise prevented, e.g., by the absorption of oxygen and ozone at wavelengths shorter than about 190 nm. For single color two-photon absorption at photon energy $\hbar\omega$, the probed wavelength would then be $2\hbar\omega$, corresponding to half the excitation wavelength. For single photon transitions, the selection rules state that the initial and final states must have different parity, e.g., S–P, P–D are allowed transitions. In contrast, for two-photon transitions the parity of the initial and final states must be the same, e.g., transitions between two S states are allowed, whereas transitions between S and P are forbidden.

In Paper I, single-color, two-photon laser-induced fluorescence was employed in order to

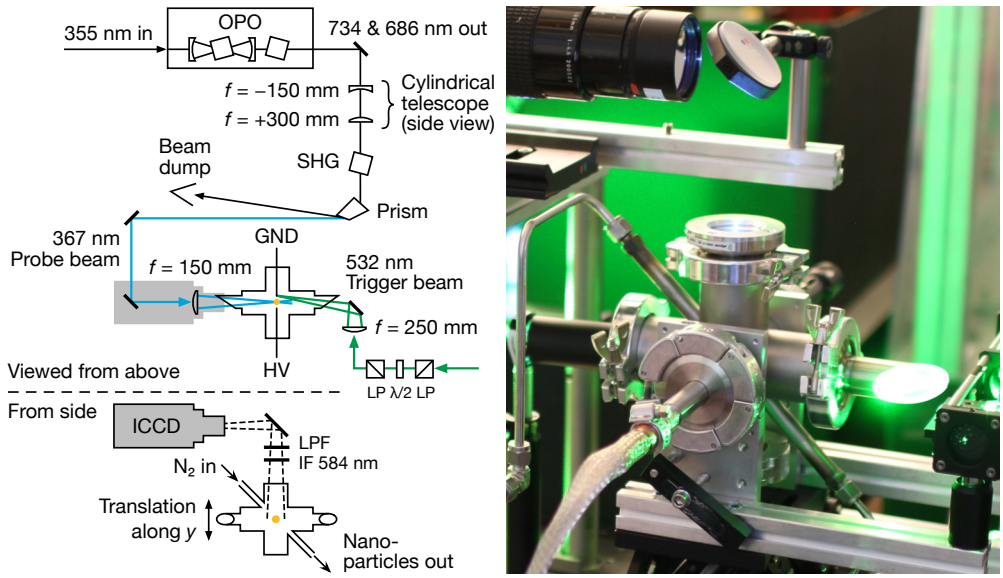

Figure 2.8: Left: Optical setup for two-photon laser-induced fluorescence. The discharge chamber can be translated along the line of sight, i.e., in and out of the figure plane, above the dashed line, or up and down, below the dashed line. The probe beam enters the discharge chamber from the left, and the trigger beam (green) from the right. **Right:** Shown to the right is a photograph of the two-photon LIF setup.

excite a transition at 183 nm, by absorption of two 367 nm photons. The resulting fluorescence will then be emitted in a wavelength range with less interference from the strong plasma background emission in the UV. The experimental setup used in Paper I is shown in figure 2.8. A pulsed optical parametric oscillator was used for exciting the two-photon transition at 367 nm from the 6s ground state to the 7s excited state, from which emission at 584 nm and 751 nm is emitted when relaxing to the 6p states. The excitation beam was focused between the electrodes, and the 584 nm fluorescence was detected through the top window of the discharge chamber.

The discharge channel can be imagined as a cylinder along the horizontal axis connecting the two electrodes (let's call it the x-axis). By translating the the discharge chamber vertically in 0.5 mm steps, and collecting images, looking down the translation axis (y-axis) at each step, a two-dimensional, cross-sectional view of the gold distribution in the yz-plane is obtained if the individual one-dimensional images are stacked side by side, as shown in figure 2.9 for different delays after breakdown and different supply voltages.

The images thereby visualize the radial expansion of the gold vapor plume, which exhibit dark concentric minima. Generally, higher voltage (discharge energy) results in higher two-photon LIF intensity (gold atom number density), and larger plume radius at a given time

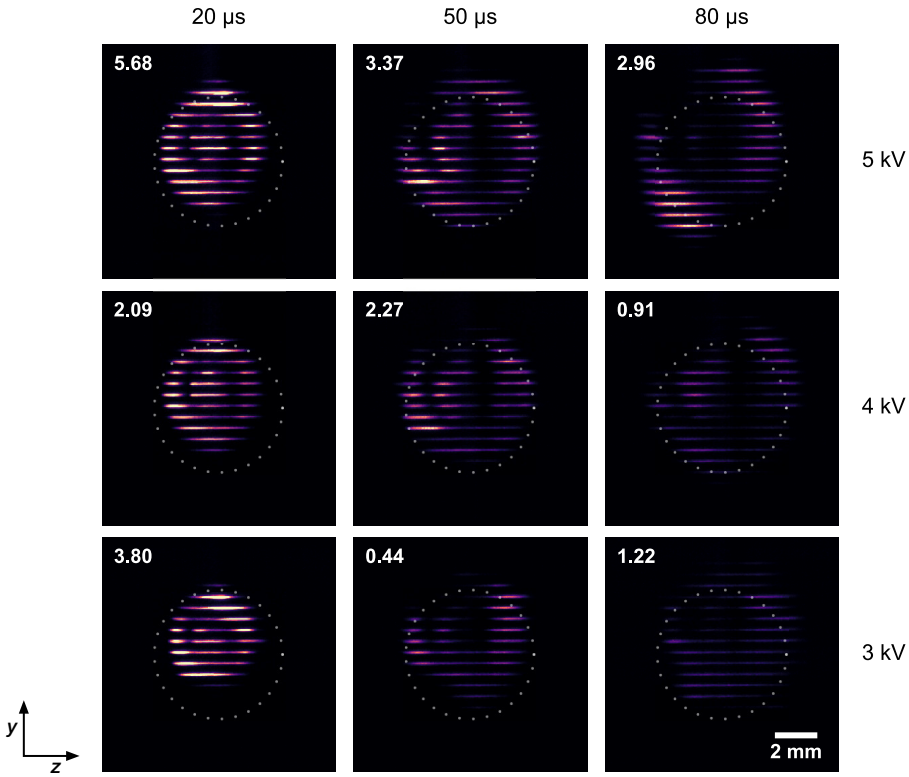

Figure 2.9: Two-photon laser induced fluorescence of gold atoms at 584 nm, when excited at 367 nm. Each horizontal slice is a LIF image taken with the discharge chamber displaced by 0.5 mm along the line of sight of the camera (along the y axis). The number in each frame is the integrated intensity, and the dots indicate circles with 6 mm diameter.

after breakdown. The volume and concentration of the initial metal vapor cloud can be used for modeling the nanoparticle formation process. [22] It can be concluded that two-photon LIF at 367 nm is feasible for detecting and visualizing the gold atom distribution of the vapor plume ablated from the electrodes, despite strong background emission from the spark discharge plasma.

4 Particle characterization

So far the description has concerned the discharge, and the ablated gold vapor cloud, without including the gold particles that are generated as the vapor condenses. This section is a summary of particle sampling measurements performed to characterize the gold particles generated by the spark discharge aerosol generator. This was done in order to scale the gold

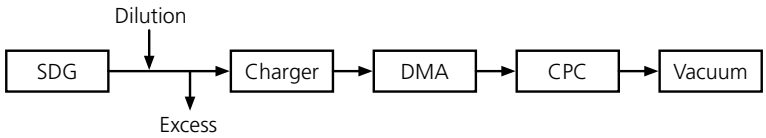

Figure 2.10: Measurement of particle size distribution using a scanning mobility particle sizer (SMPS)

nanoparticle photoluminescence signal as reported in Paper II, and discussed in more detail in chapter 3.

In order to characterize the particles generated by the spark discharge generator, the number density and size distribution of gold particles generated were measured off-line, using a scanning mobility particle sizer (SMPS). Shown in figure 2.10 is a schematic overview of the system, which consists of a bipolar charger, a differential mobility analyzer (DMA, model 3081, TSI), and a condensation particle counter (CPC, model 3775, TSI). The charger contains a Ni-63 sample which emits β-radiation, giving the particles a known charge distribution. For 30 nm diameter particles, most of the particles that has passed the neutralizer will be neutral, whereas about 16 % will have a negative charge, and 12 % a positive charge. [23, 24] The DMA acts as a tunable size filter for either the positive or negatively charged particle fractions. Using a variable electric field, particles that falls within a narrow mobility size distribution are deflected such that they are transmitted, whereas larger or smaller particles are rejected. For spherical particles, the mobility diameter reduces to the actual particle diameter. The CPC counts the remaining particle fraction optically. By scanning the pass-band of the DMA, the particle size distribution is obtained. The result for 2 mm spark gap and 5 mA charging current is shown in figure 2.11.

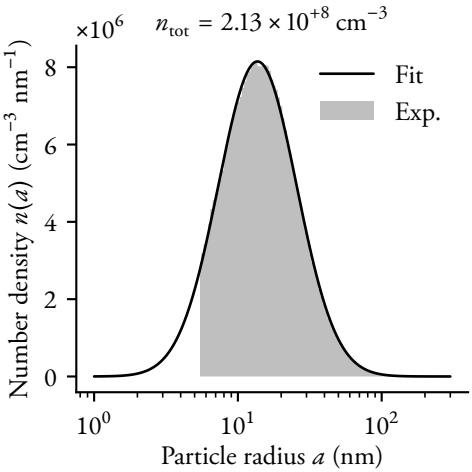

Figure 2.11: Particle size distribution of gold nanoparticles generated in the spark discharge generator at 2 mm spark gap (filled gray curve). The solid black curve is a log-normal fit to the size distribution.

Chapter 3

Optical detection of metal nanoparticles in aerosol environments

A flow of gas-borne nanoparticles offers unique possibilities for optical measurements. The most obvious way to detect small particles in aerosol phase is by their elastic scattering (Mie scattering), because it is how we perceive them with the naked eye. The absolute detection limit is then determined by the elastic scattering from any other particulate matter and Rayleigh scattering of the carrier gas. The relative intensities of Mie scattering from gas-borne gold nanoparticles, and the Rayleigh and Raman scattering from nitrogen is illustrated in figure 3.1. A common way to increase selectivity is to detect the inelastic scattering (Raman) or non-resonant fluorescence (photoluminescence) at a wavelength different from the excitation wavelength. Detection of photoluminescence from gold, silver, and copper nanoparticles suspended in a flow of nitrogen was demonstrated in Paper II. The intensity of the photoluminescence signal from gold nanoparticles was scaled by the Raman signal from the nitrogen carrier, and the particle size distribution, which enabled the determination of the photoluminescence quantum yield. Whereas Mie scattering responds to the particle surface, photoluminescence is a volume effect, and has the potential to probe the band structure of the material. Like absorption, the photoluminescence signal scales with the particle radius a as a^3, making it a promising candidate for quantitative measurements of the total particle mass. This could be important in optical diagnostics on gas-phase metal nanoparticle growth and alloying, which is discussed in chapter 5.

Photoluminescence in metals was first reported in the 1960s, manifesting as weak broadband emission from metal surfaces excited with a narrowband laser. [25] The process was interpreted as the excitation of d-band electrons to the sp conduction band, from where they relax, and the photoluminescence is emitted during radiative recombination of electrons and holes. In general the reported quantum efficiency for photoluminescence emission

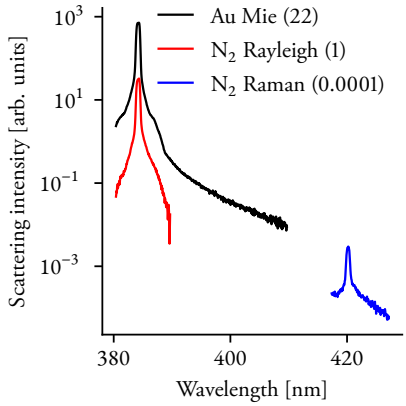

Figure 3.1: Relative intensity of Mie scattering from airborne gold nanoparticles, and molecular Rayleigh and Raman scattering from nitrogen, when excited at 385 nm. The respective scattering intensities, integrated over the instrumental function of the spectrometer, are given within parentheses. The gold nanoparticles were generated using the method described in chapter 2, and the size distribution is shown in figure 2.11. The spark gap was 2 mm, and the charging current setpoint was 20 mA.

from smooth bulk metal surfaces is very low, in the order of 10^{-10}, a likely reason photoluminescence in metals has not historically attracted much attention. Rough surfaces and nanoparticles were found to have much higher quantum efficiency however, in the order of 10^{-7} to 10^{-6}, which greatly increases its potential use as a diagnostic tool. There are two main explanations for the phenomenon in the literature. Studies of rough gold surfaces illuminated with a CW laser resulted in an enhancement of the photoluminescence signal which was attributed to a local field enhancement effect, analogous to surface enhanced Raman spectroscopy (SERS). [26, 27, 28] Instead of surface enhancement, an alternative theory for plasmonic nanoparticles explains the photoluminescence emission as the creation of a particle plasmon following nonradiative recombination of the electrons and holes. The particle plasmon is emitted as a photon, and the photoluminescence emission spectrum was reported to closely follow the calculated Mie extinction efficiency of the particles. [29]

1 Experimental setup

Shown in figure 3.2 is the experimental setup used in Paper II for detection of the photoluminescence from airborne gold, copper, and silver nanoparticles. The particles were generated in a spark discharge nanoparticle generator, described in chapter 2, and are carried in a flow of nitrogen to the optical setup. The excitation laser beam crossed the nanoparticle-laden carrier gas flow in open air. In order to reduce interference from dust particles and oxidation, the carrier gas was shielded by a flow of nitrogen.

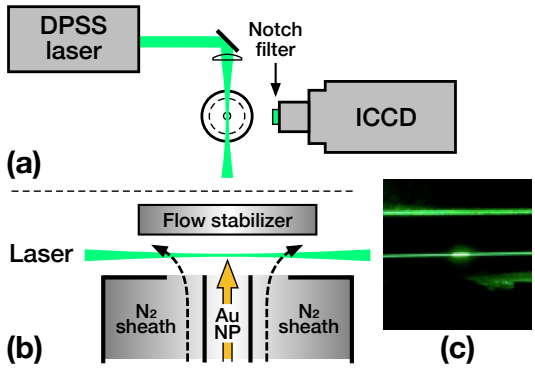

Figure 3.2: Experimental setup for detection of photoluminescence from gas-borne gold nanoparticles **(a)** as viewed from above, and **(b)** from the side, as seen by the ICCD. Gold nanoparticles, generated by spark ablation are carried in nitrogen and shielded by a surrounding nitrogen flow. The particles were excited by a 15 W CW DPSS laser at 532 nm, focused at the particle stream, and the resulting photoluminescence was collected using an intensified CCD (ICCD) camera perpendicular to the laser beam and particle flow direction. Elastic Mie scattering from the particles is blocked by a notch filter. Shown in **(c)** is a photograph of the experimental setup as viewed from the ICCD. The central bright spot is the strong Mie scattering from gold nanoparticles.

The particles were excited at 532 nm using a continuous wave (CW) diode-pumped solid-state (DPSS) laser (Sprout 15 W, Lighthouse Photonics). The beam waist diameter was approximately 90 µm. The resulting photoluminescence emitted by the particles were collected using an intensified CCD camera (ICCD). A narrow notch filter blocked the elastic Rayleigh scattering from the carrier gas, and Mie scattering from the particles, while transmitting the much broader photoluminescence emission, and the nitrogen Raman signal. For spectrally resolved measurements, the ICCD was mounted on a spectrometer (SP150, Princeton Instruments), and the photoluminescence emission was imaged 1:1 on the horizontally oriented slit using a 100 mm focal length, 50 mm diameter lens.

2 Results and analysis

Shown in figure 3.3 is the spectrally resolved photoluminescence from gold nanoparticles for different laser polarizations, both using 15 W laser power. The dip at 532 nm is caused by the notch filter, and the peak near 607 nm is the Raman scattering from the nitrogen carrier gas. The broad spectral structure (red curve) is the photoluminescence signal. Also shown is the signal with the nanoparticle generator turned off (black curve), leaving only the nitrogen Raman signal. In contrast to Rayleigh, Raman, and Mie scattering, photoluminescence lacks polarization dependence, reflecting its volumetric origin.

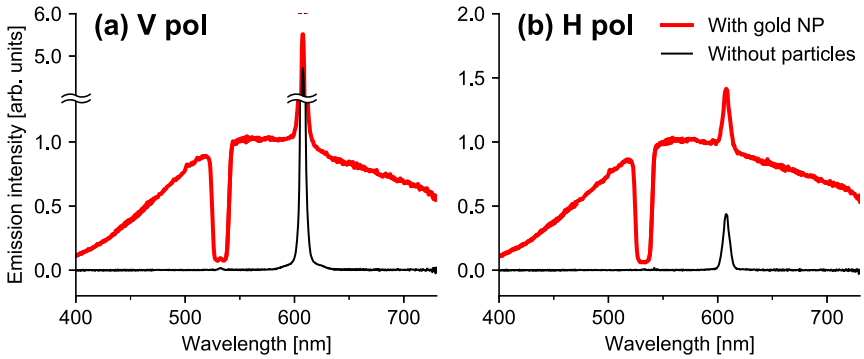

Figure 3.3: Spectrally resolved photoluminescence from gold nanoparticles (red curve), when the laser polarization is **(a)** perpendicular, and **(b)** parallel to the imaging plane. The black curve is the signal with the spark discharge generator turned off. The dip at 532 nm is caused by the notch filter blocking elastic light scattered by the excitation laser at 532 nm. The nitrogen Raman signal is seen at 607 nm.

Shown in figure 3.4 (a) and (b) are the respective spectrally integrated and spectrally resolved dependence of the gold nanoparticle photoluminescence on the excitation laser intensity. The photoluminescence emission is linear in the laser intensity except at the lowest intensity used. Similarly, the shapes of the photoluminescence spectra collected at different intensities are virtually identical. Both are indications that the emission is caused by photoluminescence and not another kind of incoherent emission, e.g., Planck radiation which has a strong T^4 dependence on temperature, and on laser intensity.

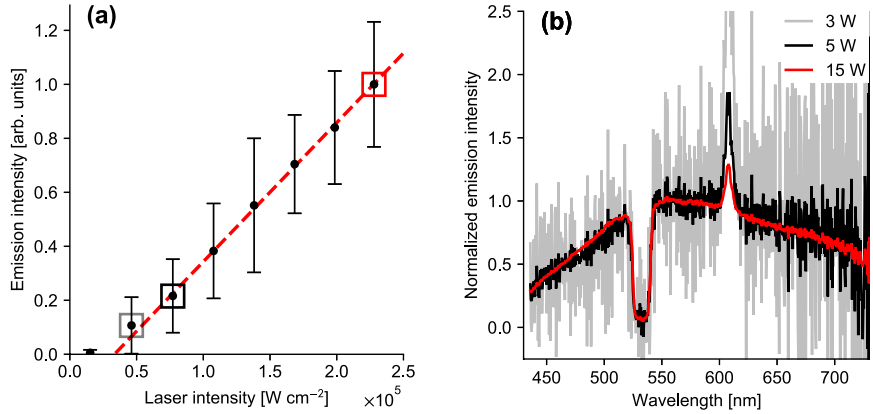

Figure 3.4: Photoluminescence emission dependence on laser intensity, **(a)** spectrally integrated, and **(b)** spectrally resolved. The values in (a) surrounded by squares correspond to the three spectra in (b).

3 Discussion

The rate of particle-assisted nanowire growth has a strong temperature dependence, and illuminating the gold nanoparticles with a continuous laser likely results in heating of the particles. This raises the question regarding the temperature of the particles as a result of laser excitation and whether laser heating can be used to influence the catalytic effect. Experimental details about the absorption and emission of thermal radiation from small (nm-sized) gas-borne metal particles are still lacking, of relevance both for fundamental and applied research, e.g., for gas-phase diagnostics on nanowire growth, and in particle trapping experiments. [30, 31, 32] Nanoparticles suspended in an inert medium with low thermal conductivity, and without optical interference, such as in nitrogen, is an ideal environment to study photo-thermal properties of nanoparticles. The absorption and emission of light by plasmonic nanoparticles is illustrated in figure 3.5.

For spherical gold particles of radius a, the power absorbed from the laser field can be estimated using Mie theory, if the dielectric function of the bulk metal is known. Collective oscillation of the conduction electrons of the particles due to an incident laser field gives rise to surface plasmons, resulting in increased absorption and scattering of light around 500 nm. [33, 34] A large imaginary refractive index at wavelengths shorter than the interband absorption edge, on the short-wavelength side of the plasmon resonance, means that light is strongly absorbed in this region. On the long wavelength side of the plasmon resonance, the absorption drops quickly and with the consequence that gold nanoparticles can be expected to absorb very little light in the near infrared, which should be considered when choosing the heating laser wavelength. From steady-state energy balance considera-

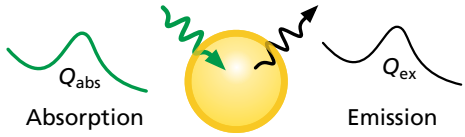

Figure 3.5: Absorption and emission of light by a plasmonic nanoparticle. The absorption cross section is proportional to the Mie absorption efficiency $Q_{abs}(\lambda)$, and peaks near the plasmon resonance around 500 nm for gold. The energy absorbed by the particle is re-emitted by formation of a particle plasmon, and the spectral profile of the emission follows the Mie extinction efficiency $Q_{ext}(\lambda)$. [29] The light is thereby coupled into and out of the particle through the plasmon resonance, resulting in a characteristic material- and size-dependent spectral profile. For a 30 nm diameter gold nanoparticle in air, $Q_{ext} \approx Q_{abs}$.

tions, the power absorbed and dissipated from each particle must satisfy

$$W_{laser} - W_{rad} - W_{cond} = 0, \tag{3.1}$$

where

$$W_{laser} = \sigma_{abs} I_{laser}, \qquad \text{Laser heating term} \tag{3.2}$$

$$W_{cond} = 4\pi\kappa a(T_a - T_0), \qquad \text{Thermal conduction to the medium} \tag{3.3}$$

$$W_{rad} = 4\pi a^2 \varepsilon\sigma(T_a^4 - T_0^4). \qquad \text{Planck radiation (large particles)} \tag{3.4}$$

Here T_a is the particle temperature, and T_0 the ambient temperature. Planck (thermal) radiation can usually be neglected ($W_{rad} \ll W_{cond}$), and the steady state temperature rise is given by

$$T_a - T_0 = \frac{\sigma_{abs} I_{laser}}{4\pi\kappa a}, \tag{3.5}$$

where σ_{abs} is the absorption cross section at the excitation wavelength λ_{ex}, calculated using Mie theory for spherical particles using dielectric function of gold, $I_{laser} = P_{laser}(\pi w_0^2)^{-1}$ the laser intensity for incident power P_{laser} and beam waist radius w_0, $\kappa = 25\,\mathrm{mW\,m^{-1}\,K^{-1}}$ the thermal conductivity of nitrogen, and a the particle radius. For an 80 nm gold nanoparticle, the absorption cross section at 532 nm is approximately $\sigma_{abs} \approx 5.6 \times 10^{-15}\,\mathrm{m^2}$. Outside the particle, the temperature can be calculated analytically, e.g., using the approach in Ref. [35], or using numerical methods. The time dependence (necessary if using short laser pulses) is usually modeled using a two-temperature model, which considers electron temperature and lattice temperature separately. [36, 37] Shown in figure 3.6 is the simulated temperature of a 80 nm gold nanoparticle inside a 15 W laser beam using a 90 µm beam waist diameter.

The above is true at moderate temperatures. As the temperature approaches the boiling point more and more of the gold will be in vapor phase, the sizes of the particles are reduced, which would reduce their absorption cross section, allowing them to cool down. This

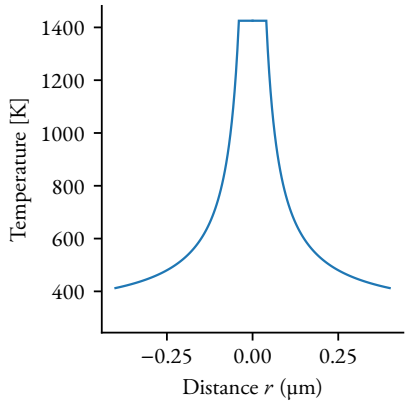

Figure 3.6: Estimated temperature around a 80 nm-diameter gold nanoparticle in air, as a function of the radial coordinate r, with $r = 0$ at the center of the particle. The laser parameters were: 15 W, 90 µm beam waist diameter, 532 nm wavelength. The solid blue curve was calculated using the analytical model from Ref. [35].

suggests that there should be a balance between these two processes at a given (CW) laser intensity and temperature. A relative reduction in particle size of a stream of gas-borne metal nanoparticles could be determined from the reduction in Mie scattering, which scales as a^6, where a is the particle radius.

A couple of different experimental approaches are proposed below to validate or estimate the temperature of gas-borne nanoparticles.

For spherical particles which are large compared to the wavelength of light, with a known spectrally independent emissivity, the temperature could be estimated based on their thermal emission, using Planck's law. The peak of the blackbody curve is given by Wien's displacement law, and for moderate temperatures the emission would end up in the near- and mid-infrared. Gold has a melting point of 1 337 K and a boiling point of 3 243 K, resulting in thermal emission maxima at around 2 µm and 900 nm, respectively, assuming the particles act like blackbodies with emissivity $\varepsilon = 1$, independent of wavelength.

A better estimate for large particles may be obtained by calculating the (spectral) emissivity using Mie theory. A summary of results from Mie theory relevant to the discussion are included at the end of this chapter. The Mie absorption efficiency $Q_{\text{abs}} = Q_{\text{abs}}(\lambda)$ of a spherical particle is defined as the ratio between the absorption cross section and the geometric cross section of the particle, $\sigma_{\text{geom}} = \pi a^2$, at the wavelength λ. Thus Q_{abs} is an unitless quantity expressing the fraction of the incident light absorbed by the particle. This is the same definition as emissivity ε, so under conditions when Planck's law applies, i.e., for particles of the same dimension as the thermal emission wavelength or larger, it must hold that the spectral emissivity of a spherical object equals its absorption efficiency. Shown in

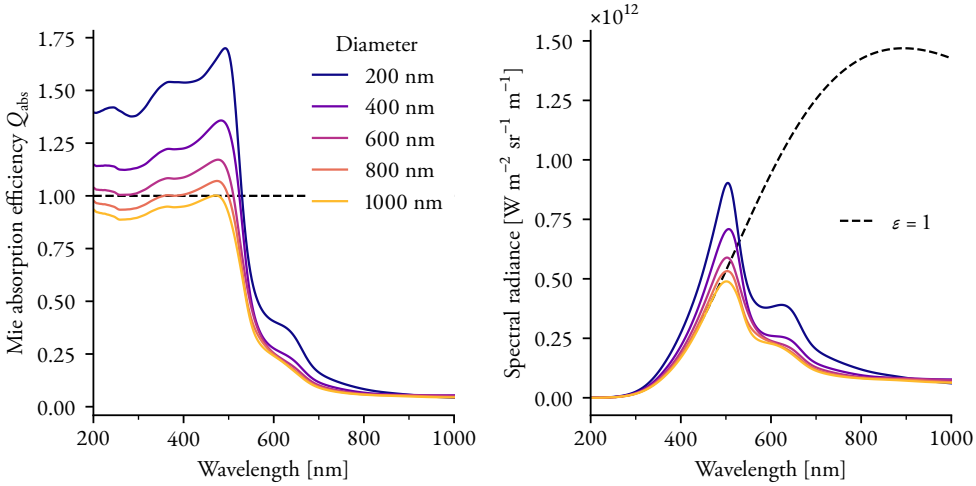

Figure 3.7: **Left:** Calculated Mie absorption efficiency Q_{abs} for different gold particle sizes. **Right:** calculated Planck emission spectrum for particles with $\varepsilon = Q_{abs}$ at the boiling temperature of gold. The broken curve is the corresponding blackbody spectrum.

figure 3.7 (left) is the calculated Mie absorption efficiency Q_{abs} for particles with diameter between 200 nm and 1 µm. Using $\varepsilon(\lambda) = Q_{abs}$, the corresponding Planck emission curves are obtained, as shown on the right hand side, for gold nanoparticles in air near the boiling temperature.

An alternative to measuring the Planck emission directly, while avoiding the issues regarding its possible validity for small particles, would be to measure the amount of gold atoms evaporated from the particles, e.g., using laser-induced fluorescence. The LIF signal would then be subject to the vapor pressure of gold, to a first approximation estimated by the temperature surrounding the particle, cf. figure 3.6. The concentration would be higher closer to the particle due to the temperature gradient, depending on the thermal diffusivity of the medium, and the temperature of the gold atom cloud surrounding the particle would be a lower bound to the particle temperature. The temperature of the gold atoms could in principle be determined from the Doppler broadening of the absorption lineshape. Due to the much larger (factor 10) collisional broadening at atmospheric pressure, one would likely have to rely on the intensity of the observed LIF emission. This could be calibrated, e.g., in a flame or in a furnace. Due to the Kelvin effect, [38, 39] the vapor pressure is increased for smaller particles compared to the bulk material. The laser beam width should be chosen to exceed the inter-particle distance, and ideally, the inter-particle distance should also exceed the spatial resolution of an imaging system.

By increasing the dilution of the particle flow, eventually the optical response corresponds to individual particles, rather than the aerosol volume as a whole. By taking this concept

to the extreme, single particles could be studied over time in a trap. Trapping of gold nanoparticles in air has been demonstrated, using optical tweezers [30] and using a radio-frequency ion trap or Paul trap, [32, 40] however, for the particle sizes considered, the trapping frequencies would be in the order of kHz. Especially, the linear Paul trap [41, 42] is an attractive option for particles with a known charge, as the trap itself then acts as a size-selective filter, with a stability region determined by the mass-to-charge ratio of the particles and the chosen trap frequency and voltages. An advantage over optical trapping is that the trapping and excitation/detection mechanisms are decoupled, relaxing the requirements on the manipulating or excitation laser beams. This flexibility also allows a wider range of possibilities regarding choice microscope objective, e.g., reflective objectives can be used, allowing broadband spectroscopy.

4 Some results from Mie theory

The optical properties of spherical metal particles can be described using Mie theory. The Mie cross sections for light incident on a spherical particle are derived by solving Maxwell's equations in spherical geometry. Only the results of interest for practical use and for the discussion will be reproduced here; a full derivation of Mie theory can be found in standard works like Ref. [43] and [44].

The Mie efficiencies Q are defined as the ratio between the respective cross section σ and the geometric cross section of a spherical particle, i.e., the area of a disk with the same radius a as the particle. Thus the Mie scattering cross section is given by $\sigma_{\text{sca}} = Q_{\text{sca}}\pi a^2$. In the far-field limit, the solution for the scattering, absorption and extinction efficiencies, integrated over all angles, is

$$Q_{\text{sca}} = \frac{2}{x^2}\sum_{n=1}^{\infty}(2n+1)(|a_n|^2 + |b_n|^2), \tag{3.6}$$

$$Q_{\text{ext}} = \frac{2}{x^2}\sum_{n=1}^{\infty}(2n+1)\,\text{Re}(a_n + b_n), \tag{3.7}$$

$$Q_{\text{abs}} = Q_{\text{ext}} - Q_{\text{sca}}, \tag{3.8}$$

where the Mie coefficients a_n and b_n are given by

$$a_n = \frac{\psi_n(x)\psi_n'(y) - m\psi_n'(x)\psi_n(y)}{\zeta_n(x)\psi_n'(y) - m\zeta_n'(x)\psi_n(y)}, \qquad b_n = \frac{\psi_n'(x)\psi_n(y) - m\psi_n(x)\psi_n'(y)}{\zeta_n'(x)\psi_n(y) - m\zeta_n(x)\psi_n'(y)}, \tag{3.9}$$

and

$$x = \frac{2\pi a}{\lambda}, \qquad \lambda = \frac{\lambda_{\text{vacuum}}}{m_{\text{medium}}},$$

$$y = mx, \qquad m = \frac{m_{\text{sphere}}}{m_{\text{medium}}}.$$

Here λ is the wavelength of light in the medium, and m the relative or effective refractive index. The functions $\psi_n(z)$ and $\zeta_n(z)$ are the Riccati-Bessel functions. These are related to the spherical Bessel and Hankel functions, and the Bessel and Hankel functions of the first kind:

$$\psi_n(z) = z j_n(z) = (\pi z/2)^{1/2} J_{n+1/2}(z), \tag{3.10}$$

$$\zeta_n(z) = z h_n^{(1)}(z) = (\pi z/2)^{1/2} H_{n+1/2}^{(1)}(z). \tag{3.11}$$

The size parameter x expresses the ratio between the particle size and the wavelength of light in the medium, and determines the number of series terms that are required for convergence. Typically, Mie theory is appropriate when x is on the order of unity. When $x \ll 1$, we are in the Rayleigh regime, and when $x \gg 1$ we are in the geometrical optics regime. Note that the size parameter depends on the relative refractive index. This explains why Mie theory is typically required to model the optical properties of metal nanoparticles (with large imaginary index of refraction), even though they can be much smaller than the wavelength of light, which is the conventional criterion for dielectric particles.

Chapter 4

Pyrolysis and photolysis of trimethylindium (TMIn)

When trying to understand a complex process, it is instructive to first understand its constituent processes. As an example, the growth of InP requires mixing gold particles with trimethylindium [TMIn, $(CH_3)_3In$] and phosphine at high temperature. This chapter focuses on the behavior of TMIn alone, and its release of indium atoms, when heated or exposed to deep ultraviolet laser light. TMIn is one of the most important metal-organic precursors for providing indium in metal-organic vapor phase epitaxial (MOVPE) processes. However, the spectroscopy of TMIn is quite complex, and it possesses no known fluorescence. On the other hand, using high resolution laser spectroscopy, we can measure free indium atoms with high sensitivity. More specifically we can image their distribution using laser-induced fluorescence, and measure their concentration using absorption spectroscopy. This makes the indium atom a useful marker for concentration and temperature distribution for indium-containing species across the temperature range of interest for nanowire growth, without having to rely on techniques that require introduction of foreign species, thereby influencing the chemical processes under study. The focus of this study is therefore on optical diagnostics on indium-related semiconductor nanowire growth processes and the chemical environment in which they take place, however, the proposed techniques should be adaptable to other aerotaxy or MOVPE processes, by different choice of excitation and detection wavelengths. Using indium atoms as markers for other species that are more difficult to detect, e.g., because of their spectroscopy, or only exist in trace amounts, and by intelligent choice of excitation wavelength we can choose which species to target, ideally without affecting the others. Shown in figure 4.1(a) is an overview of the absorption spectra of some metalorganic precursors commonly used in III–V semiconductor growth, which are all characterized by broad absorption features in the deep ultraviolet.

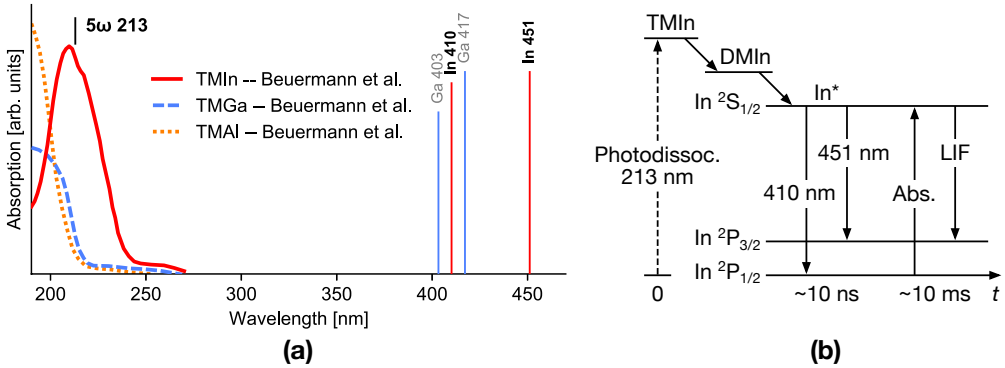

Figure 4.1: **(a)** Spectral overview of the absorption spectra of some group III metal-organic precursors and the respective metal atoms. Absorption spectra of TMIn, TMGa, and TMAl were obtained from Ref. [45]. **(b)** Partial energy diagram of the indium atom and the proposed detection scheme for photodissociation of TMIn by laser-induced fluorescence detection of the indium fragments. Dimethylindium (DMIn) and methyl fragments are produced by pulsed photodissociation of TMIn at 213 nm, which quickly decomposes into indium and ethane. [45] Shortly after the dissociation pulse, indium atoms that are produced in an excited state (In*) fluoresce at 410 nm and 451 nm. The ground state indium atoms are probed using a CW laser at 410 nm, as much as 25 ms after the photodissociation pulse, depending on temperature, and the non-resonant LIF is detected at 451 nm.

In the specific case discussed here, indium is produced by ultraviolet photodissociation of TMIn at a wavelength that the precursor is known to absorb, but not other species, and the precursor can then be targeted specifically, since photolysis will then be the only source of the fragment metal atoms. The proposed detection scheme is illustrated in figure 4.1(b). In chapter 5, a conceptually similar approach is proposed for the detection of indium alloy particles, demonstrating that the technique is not limited to detection of gas-phase species.

Indium atoms were generated by combination of two different mechanisms, pyrolysis and photolysis—the ratio between the two given by the temperature—and a combination of two different techniques was used for measuring the indium atom fragments. Laser-induced fluorescence provides the possibility of highly sensitive imaging, and absorption spectroscopy provides the indium concentration estimated using Beer's law. By combining the two techniques the indium atom distribution, and by extension TMIn, can be imaged quantitatively in the reactor with high sensitivity and specificity, as demonstrated in Paper III. The equilibrium concentration of indium atoms at a given temperature is given by the vapor pressure of indium. However, since TMIn is continuously provided by the gas flow, and indium is continuously produced by pyrolysis and photolysis, the system is never at equilibrium. Since the vapor pressure of TMIn is much higher than that of free indium, the resulting indium concentration directly following photodissociation is also initially higher, as long as the TMIn decomposition rate is sufficiently fast.

At moderate laser intensities, the sudden increase in indium concentration due to pulsed photodissociation is sufficient to create a super-saturation of indium vapor resulting in the formation of a visible particle cloud. The phenomenon itself is not new, [46] but this is the first time being reported for metal-organic precursors, and it raises a number of questions regarding the composition of the particles and their properties, and whether this can be used for controlling the aerotaxy process. Based on the gas temperature at which the phenomenon occurs, it is likely that the observed particles are liquid indium droplets. Liquid indium or gallium droplets or even wires are commonly encountered at high precursor concentration at typical aerotaxy growth temperatures, but that is a passive, parasitic effect. The spatial, temporal, spectral and intensive control granted by pulsed laser-induced particle generation could make this a valid target for further studies.

In this chapter the pyrolysis and photolysis of TMIn are studied in an environment simulating aerotaxy conditions, provided by an open-air flow reactor designed to allow unrestricted optical access to the hot reactant flow. In section 1 the reactor is described, as well as the experimental setup used for measurement of indium atoms generated in the reactor by pyrolysis of TMIn, and from photodissociation by a pulsed ultraviolet laser. In section 2 and section 3, respectively, the results from the pyrolysis and photolysis experiments on TMIn are reviewed, which were reported in Paper III.

1 Experimental setup

1.1 Pyrolysis reactor

In order to study the pyrolysis and photolysis processes of TMIn, a flow reactor was designed, with special emphasis on optical accessibility, allowing sufficient temperature range to cover typical aerotaxy conditions. Shown in figure 4.2 is a schematic illustration of the flow reactor and the metal-organic (MO) vapor delivery system. The solid or liquid MO precursor is kept in a container with one inlet and one outlet, placed in a temperature-controlled bath. In order to deliver MO vapor to the reactor, an inert carrier gas is flowed through the precursor. At moderate flow rates, typically less than $0.5\,\mathrm{L\,min^{-1}}$, the carrier gas will be saturated with MO vapor at a concentration determined by its saturated vapor pressure and temperature, which is usually fixed at below room temperature to avoid condensation. The MO vapor is carried to the reactor where it is heated electrically, up to approximately 1 000 °C. A thermocouple mounted inside the heater provides temperature feedback. The optically accessible probe region is located between the heater tube and a flow stabilizer, mounted approximately 20 mm above the heater tube exit. Once the flow exits the heating tube, it is shielded by nitrogen, preventing contamination by the surrounding air and dust particles.

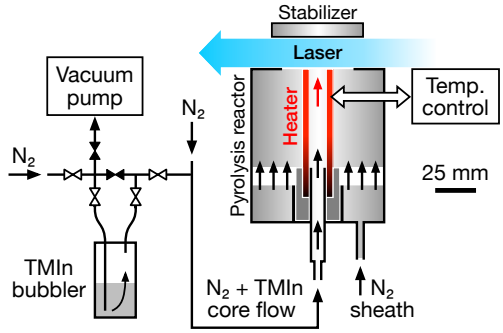

Figure 4.2: Metal-organic vapor delivery system and pyrolysis reactor. TMIn vapor is delivered to the reactor by flowing nitrogen through solid TMIn. The reactor heats the reactant TMIn + N_2 flow electrically using a ceramic heating element. A surrounding sheath flow protects the reactant flow from oxidation once it enters the optical probe region, located between the reactor and a flow stabilizer.

1.2 Optical setup

Quantitative measurements on the indium atoms produced by pyrolysis of TMIn was provided by high resolution absorption spectroscopy, using a CW Ti:Sapphire laser, which is described in the next section. The optical layout for TMIn pyrolysis is shown schematically in figure 4.3(a). A multipass absorption arrangement was employed to increase the absorption path length a factor 29 compared to singlepass absorption. The arrangement was composed by a concentric cavity, [47] formed by two –100 mm focal length mirrors with 50 mm diameter. Using this arrangement, no modification of the mirrors, e.g., drilling or notching, is necessary in order to accommodate the input and output beams, meanwhile the 5 mm cavity waist diameter matches the 12 mm diameter of the reactant flow well. The laser was scanned across the $^2S_{1/2} \leftarrow {}^2P_{1/2}$ transition of the indium atom near 410 nm, and the multipass absorption signal was detected on a photodiode. The indium concentration was obtained by fitting a theoretical spectrum to the absorption spectrum.

Shown in figure 4.3(b) is the optical setup for CW planar laser-induced fluorescence (PLIF) of indium atoms generated by pyrolysis. The incoming 410 nm beam was expanded vertically to a 19 mm laser sheet, intersecting the vertical gas flow above the reactor. Indium was excited ut 410 nm using the same transition used for absorption, and the non-resonant laser-induced fluorescence resulting from the $^2S_{1/2} \rightarrow {}^2P_{3/2}$ transition, was detected at 451 nm using an intensified CCD camera (ICCD).

Shown in figure 4.4 is the optical setup used for combined single-pass absorption measurements and PLIF of indium atoms, produced by a combination of pyrolysis and pulsed photolysis of TMIn at 213 nm. A strong fluorescence signal was observed from indium formed by photolysis in an excited state (In^*), during the photolysis laser pulse (in the or-

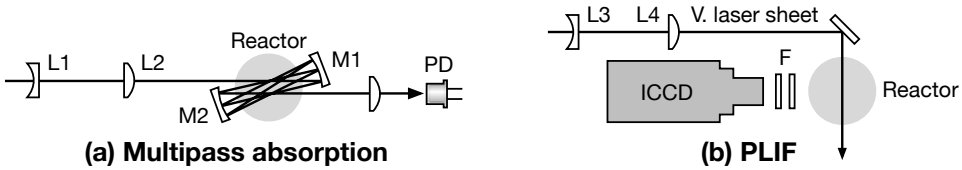

Figure 4.3: Optical setup for **(a)** multipass absorption and **(b)** PLIF of indium atoms during pyrolysis of TMIn, as seen from above. In (a), the two mirrors M1 and M2 form a concentric multipass cavity centered on the reactor. The incoming 410 nm beam is matched to the cavity using the lenses L1 and L2, and the resulting transmittance after passing through the reactant flow several times is detected using a photodiode (PD). In (b), the 410 nm beam is expanded to a 19 mm vertical laser sheet using a cylindrical lens L3 and spherical lens L4, passing through the reactant flow. L3 is seen from the side. The resulting 451 nm fluorescence is imaged on an intensified CCD camera (ICCD) through optical filters (F).

der of 10 ns). The ground state indium atoms were probed by CW absorption spectroscopy and PLIF, with the laser wavelength fixed at the absorption maximum at 410 nm, otherwise similar to as described previously for the pyrolysis measurements. Because of the much higher concentration of indium atoms generated by photolysis, only a single pass was necessary to provide sufficient indium absorption signal. The transient absorption signal was recorded on an oscilloscope.

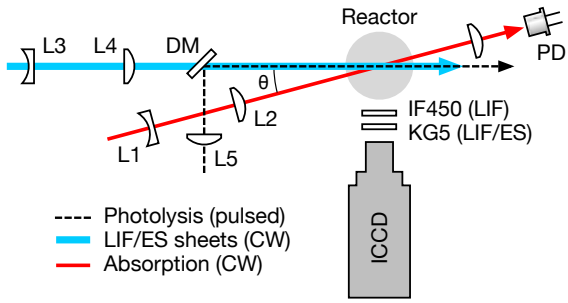

Figure 4.4: Optical setup for combined CW PLIF, elastic scattering (ES), and singlepass absorption spectroscopy of indium atoms generated by pulsed photolysis. The 410 nm, and 532 nm beams forms laser sheets passing through the reactant TMIn + N_2 flow. The 451 nm LIF following 410 nm excitation is detected through a narrowband interference filter (IF451), and a KG5 filter blocking infrared emission from the heating element. The ES is resulting from scattering by the 532 nm laser sheet is detected with only the KG5 filter. The photolysis beam is overlapped with the LIF/ES sheets using a dichroic mirror (DM). The 410 nm absorption beam crosses the laser sheets and the photolysis beam at a small angle in the reactant flow, and the transmittance is detected by a photodiode (PD).

1.3 Ti:sapphire laser

Typical aerotaxy growth conditions involves a temperature of approximately 500 to 600 °C and atmospheric pressure. Under these conditions atoms in the gas phase have absorption linewidths in the order of 10 GHz, mainly due to collisional broadening. In order to measure atomic or molecular species with high sensitivity, ideally the laser line width should match the narrow linewidths of the absorbing species, and in order to perform an excitation scan over a single absorption line, the instrumental width should ideally be negligible. Furthermore, the high peak power of pulsed lasers may be destructive to particles.

The CW laser system employed for measuring indium atoms in Paper III was based on a Ti:Sapphire laser, which will be briefly described in the following. The same laser system was used for CW absorption spectroscopy on gold atoms, reported in in Paper I.

The layout of the laser system is shown in figure 4.5. The system consists of a CW pump laser (Sprout 15 W, Lighthouse Photonics), a Ti:Sapphire laser (PSX, M Squared Lasers), and two enhancement cavities, for generating the second and fourth harmonics of the fundamental emission wavelength (ECD-X and ECD-X-Q, respectively, M Squared Lasers). A wavemeter (WS6-600, High Finesse), was used for frequency stabilization and absolute frequency reference, and and Fabry Pérot interferometer (1 GHz free spectral range, FP100, Toptica) was used as a relative frequency reference when scanning the laser wavelength. During some experiments another interferometer or spectrum analyzer was used instead (300 MHz free spectral range, Coherent).

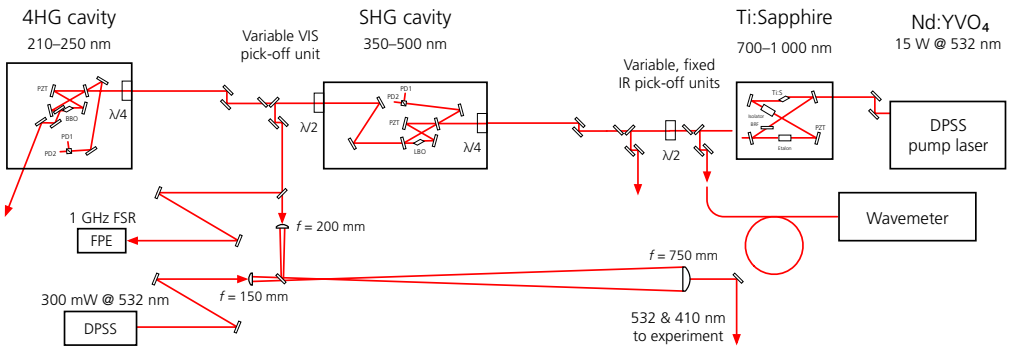

Figure 4.5: Optical layout of the continuous-wave (CW) Ti:sapphire laser system used for high-resolution absorption and laser-induced fluorescence (LIF) of indium atoms at 410 nm. Also shown is a DPSS laser used for elastic scattering by particles at 532 nm. Some optical components have been omitted from the diagram, including mode matching telescopes between the three cavities. **Legend:** SHG – second harmonic generation, 4HG – fourth harmonic generation, FPE – Fabry Pérot etalon, FSR – free spectral range, $\lambda/2$ – half wave plate, $\lambda/4$ – quarter wave plate, PZT – piezoelectric mirror mounts, BRF – birefringent filter

The gain medium of the Ti:sapphire laser is a sapphire crystal doped with titanium ions (Ti^{3+}), which has an absorption band between 400 nm and 600 nm, peaking near 500 nm, and an emission band between approximately 700 nm and 1 000 nm, with emission maximum near 780 nm. [48] The Ti:sapphire laser was pumped at 532 nm, and the fundamental emission wavelength is broadband-tunable between 700 to 1 000 nm. The maximum output power is approximately 4 W at 780 nm.

Visible light between 350 and 500 nm, and ultraviolet between 210 and 250 nm can be generated by frequency doubling the fundamental laser light first to the visible and then to the ultraviolet, using a lithium triborate (LBO) and a β-barium borate (BBO) crystal, respectively, mounted in two separate enhancement cavities. Each doubling cavity is locked to the previous cavity using Hänsch–Couillaud stabilization. [49] Whereas the fundamental cavity is relatively maintenance-free, the stability of the second and fourth harmonic laser light is determined by the respective cavity's ability to maintain lock on the previous one, and ultimately the quality of the error signals. This requires periodic optimization of coupling optics and enhancement cavities, and the frequency of this optimization has been found to be strongly correlated to the temperature fluctuations in the lab environment.

The specified emission linewidth of the laser is less than one MHz, and single-longitudinal-mode operation is maintained during a scan by simultaneously tuning the length of an intracavity etalon. Mode-hop free tuning of the fundamental wavelength is possible by altering the round-trip length of the cavity through moving one of the cavity mirrors, allowing the fundamental frequency to be scanned over some 25 GHz.

For fixed-frequency operation, the built-in control software is usually sufficient, however during mode-hop free scanning, the laser frequency has usually been controlled by applying a voltage to the *Resonator Slow External Input* terminal on the control box, directly moving the long-stroke piezoelectric mirror in the fundamental cavity. A Python program was used to communicate with the laser controllers over TCP/IP, in order to read out wavelength, enable or disable frequency stabilization, acquiring or releasing lock on the two enhancement cavities, and for data acquisition of various photodiode signals (absorption, fluorescence, power reference, etalon traces, etc.).

2 TMIn pyrolysis: Results and analysis

Summarized in this section are some results from CW laser diagnostics on indium produced by pyrolysis of TMIn, using frequency-resolved multipass absorption spectroscopy, and using fixed-frequency PLIF. The estimated TMIn concentration was approximately 300 ppm at the lower temperatures used, neglecting losses. Shown in figure 4.6(a) is an example of 29 absorption scans across the 410 nm absorption line of indium. The corresponding indium PLIF signal collected at 451 nm is shown in (b). Shown in figure 4.6(c) is the spatially integrated PLIF signal collected at different reactor temperatures, and calibrated using the absorption measurements at 600 °C. The absorption measurements thus provided a quantitative scale for the distribution of indium atoms above the reactor, obtained from PLIF measurements.

The multipass absorption spectrum shown in figure 4.6(a) was collected at 600 °C reactor temperature. The fitted spectrum indicates an indium concentration of approximately 7 ppb. This can be compared to the much lower equilibrium concentration that can be expected from the vapor pressure of indium alone, [50] which is four orders of magnitude lower than the observed concentration. The high indium concentration can be explained by the fact that indium atoms are produced continuously by pyrolysis of TMIn, which has a much higher vapor pressure than indium. [51]

It should be noted that the gas temperature in the probe region is approximately 200 K lower than the reactor wall temperature at the point where it is the highest. For this reason, the thermal decomposition of TMIn is accelerated closer to wall surfaces, which explains the two columns with higher intensity in figure 4.6(b). From Rayleigh thermometry measurements (not depicted), the gas temperature is relatively constant in the optical probe region between the reactor and flow stabilizer, and the two columns of higher indium concentration above the reactor reflects the inhomogeneous temperature distribution inside the reactor tube.

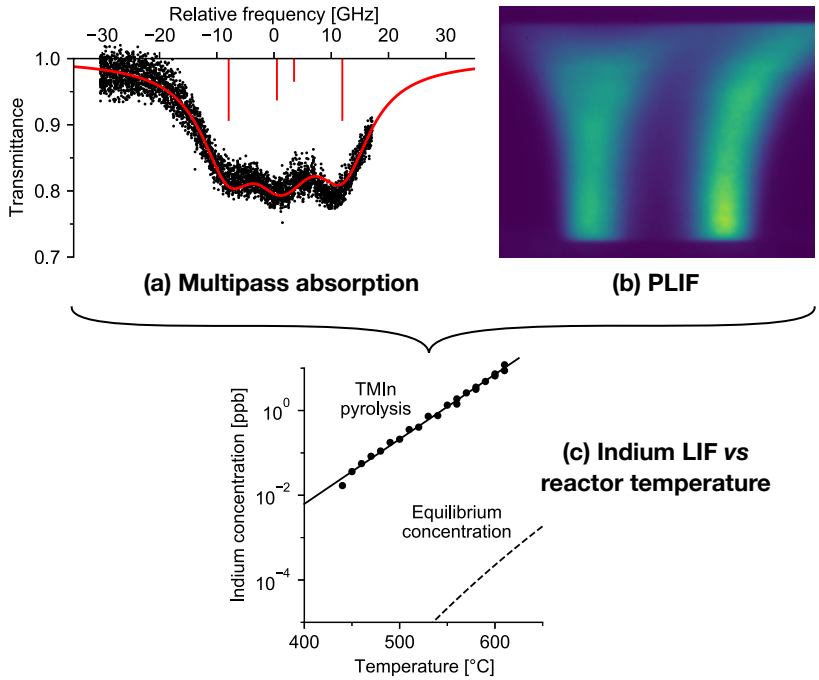

Figure 4.6: **(a)** Multipass laser absorption scan across the 410 nm indium line at 600 °C reactor temperature. The solid curve is the theoretical transmittance for 7 ppb indium concentration, assuming a Lorentzian lineshape. The vertical lines represent the relative strengths of the four hyperfine components of the transition. **(b)** Calibration of PLIF signal from multipass absorption measurements. The (false color) image depicts a cross section through the spatial distribution of indium atoms between the reactor and flow stabilizer. **(c)** Spatially integrated PLIF signal a function of reactor temperature. The vertical axis has been calibrated using the absorption measurements in (a).

3 TMIn photolysis: Results and analysis

3.1 Pulsed photodissociation

In this section the results from optical diagnostics on pulsed TMIn photolysis are presented. Measurements were performed at different reactor temperatures, i.e., indium atoms are produced by a combination of pulsed photolysis and pyrolysis, depending on the temperature. The photolysis laser coincided with the absorption maximum of TMIn at 213 nm, and the indium atoms were detected using singlepass CW absorption spectroscopy at 410 nm, using non-resonant PLIF detected at 451 nm, and by the fluorescence emitted by indium produced in an excited state as a result of the photodissociation process (In^* emission) at 451 nm.

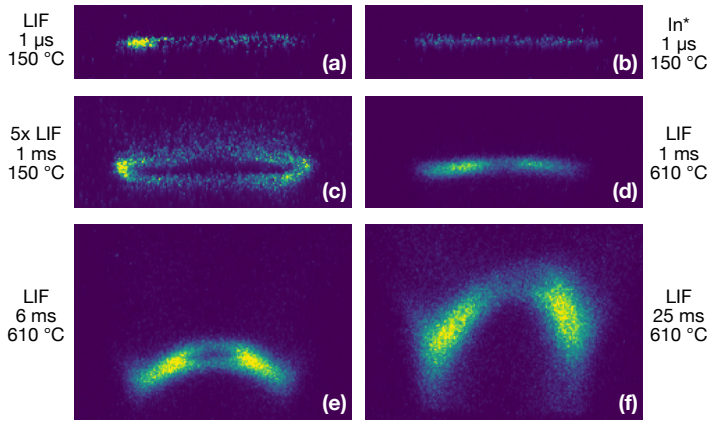

Figure 4.7: Indium laser-induced fluorescence **(a)** and **(c)–(f)**, and In* emission **(b)** during photolysis and pyrolysis of TMIn. Shown beside each figure are the delay after the photodissociation pulse and the reactor temperature used. The width of the plumes correspond to the 12 mm inner diameter of the reactor tube. Images within the same row are represented using the same color scales, except for (c), whose intensity was multiplied by a factor 5 compared to (d).

Shown in figure 4.7 are false color indium PLIF images, except for (b) which shows the much shorter-lived 451 nm emission from indium formed in an excited state. The images were collected at different delays after the photodissociation pulse, and at different reactor temperatures. Higher reactor temperatures generally result in longer lifetime of free indium atoms, possibly due to reduced number density. Conversely, a lower reactor temperature results in a higher LIF signal and a larger vapor plume at a given delay. This is most likely as a result of a higher initial indium concentration at low temperature, due to less competition with the pyrolysis process. At longer delays, >1 ms after the photodissociation pulse, the indium atoms visibly follow the gas flow, resulting in the arc-shaped vapor plumes shown in figure 4.7(e)–(f). In the center of the plume there is usually a region of lower LIF signal intensity possibly caused by depletion of indium due to condensation or ionization.

Shown in figure 4.8 are the results from measurement of single-pass indium absorption at 410 nm, following pulsed photodissociation of TMIn at 213 nm. The transient absorption signals were collected at different reactor temperatures, ranging from 200 °C to 750 °C. At each temperature, measurements were performed using 0.2 mJ, 0.5 mJ, and 1 mJ photodissociation pulse energy. The peak indium atom concentrations estimated from the absorption signals are in the order of a few ppm, which can be compared to the ppb levels obtained using pyrolysis only, without the photolysis laser. Similar to the results obtained using LIF, the lifetime of free indium atoms are generally longer at higher reactor temperature. Using a fixed photodissociation energy results in similar peak concentrations, independent of temperature. Using 1 mJ pulse energy, the indium plume starts to become optically thick.

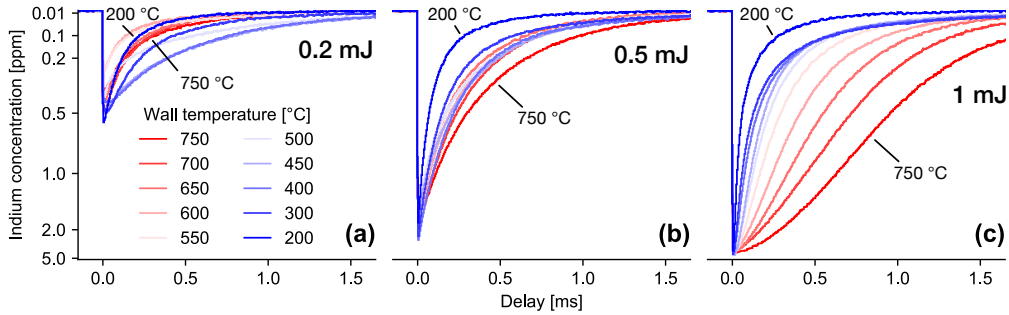

Figure 4.8: Singlepass transient absorption of indium atoms at 410 nm, using different photodissociation energies and reactor temperatures.

Finally, shown in figure 4.9 is elastically scattered light from particles generated by pulsed photodissociation of TMIn at 213 nm, at different reactor temperatures. In this imaging measurement, a 532 nm CW laser sheet was employed to visualize the aerosol particles generated from the pulsed UV laser beam. The particles are only generated along the laser beam, where it crosses the TMIn flow, and once generated, the particles follow the vertical gas flow. Each image is the result of 10 exposures, starting at 0 ms delay, and separated by 5 ms following the photodissociation pulse. Shown along the lower edge in each image is the intersection of the photodissociation laser beam with the vertical TMIn flow, resulting in strong In^* emission at 0 ms.

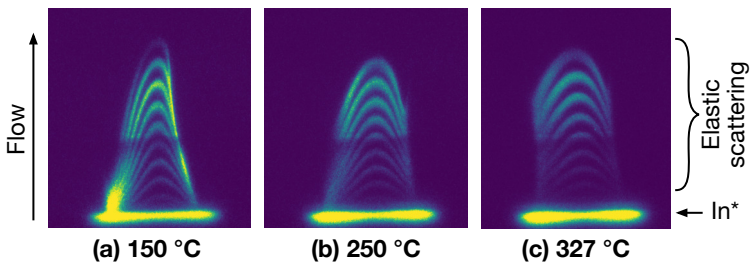

Figure 4.9: Multiple-exposure images of elastic scattering from indium droplets generated by pulsed photolysis of TMIn, at different reactor temperatures. Each image is a combination of 10 successive exposures, separated by 5 ms, following a single photodissociation pulse. Included for reference, is some of the In^* emission signal, which defines the crossing between the photolysis laser beam and the TMIn flow.

Based on the low melting point (157 °C), the high boiling point (2 072 °C), and the low vapor pressure of indium it can be expected that the particles are solid or liquid indium droplets formed by condensation of super-saturated indium vapor.

4 Discussion

The feasibility of spatially and temporally resolved PLIF measurements combined with quantitative measurements of atomic indium provided by absorption spectroscopy has been demonstrated in an environment similar to typical aerotaxy reactors. Imaging of gas-phase species in general has been historically lacking in the MOVPE community. Due to many different reactor geometries employed, the lack of imaging is a likely explanation for the large discrepancies regarding the details of the TMIn decomposition process reported in the literature. PLIF may thereby provide the necessary tool for building the necessary library of quantitative experimental data to support comprehensive kinetic modeling of aerotaxy processes, as well as MOVPE processes in general.

Using a pulsed photolysis laser adds both temporal and spatial control over the TMIn decomposition process, providing another set of dimensions to diagnostic measurements. For aerotaxy, the ability to confine the decomposition away from reactor walls may help avoiding parasitic decomposition. The fact that much higher concentration of indium atoms is achieved using photodissociation than using pyrolysis may have dramatic consequences for the growth rate.

Chapter 5

Towards in-situ optical measurement and control of the aerotaxy process

This chapter summarizes preliminary results from optical diagnostics on pyrolysis and photolysis of TMIn, and on gas-borne gold and gold–indium alloy nanoparticles, using different techniques having in common that they involve the detection of indium or gold atoms. In section 1 results from indium LIF measurements are presented, where indium atoms were produced by TMIn pyrolysis in a packed bed in order to increase the reactor surface area. In section 2 indium atoms were produced by CW photodissociation using a deuterium lamp, instead of using a pulsed laser. In section 3 gold nanoparticles in an inert gas-phase environment are studied using laser ablation combined with LIF detection of atomic fragments, and in section 4 the technique is applied to the gold–indium gas phase alloying process, with the aim to study the first stages of nanowire growth.

1 Pyrolysis of TMIn in a packed bed

Even though indium MOVPE has been studied for almost half a century, there is still no consensus about to what extent the pyrolysis of TMIn occurs homogeneously in the gas phase, or heterogeneously on surfaces. This is relevant for aerotaxy because the seed particles constitute a kind of distributed substrate. For this reason early designs for the flow reactor described in chapter 4 were designed to minimize surface area in contact with the reactants, in an attempt to study the TMIn decomposition process ideally completely in the gas phase, by eliminating any surface effects.

At the other extreme, the surface area in contact with the reactant flow could instead be

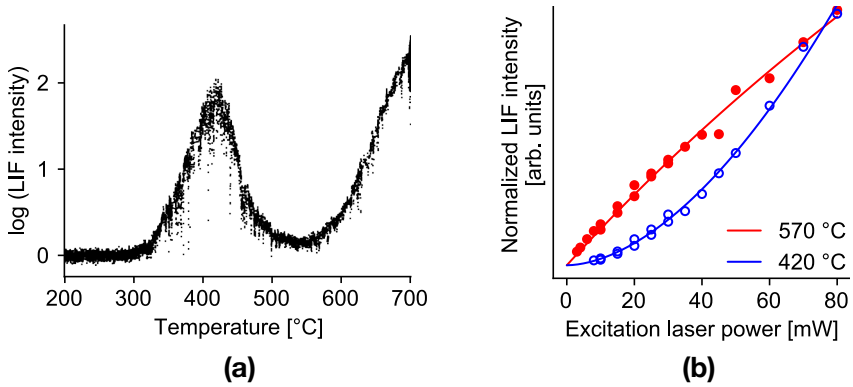

Figure 5.1: **(a)** Indium LIF signal at 451 nm during ramp-down of the reactor temperature from 700 °C to 200 °C over 8 min. The apparent noise in the LIF signal is due to the unstable flow. **(b)** Indium LIF signal as a function of the 410 nm laser power, at two different reactor temperatures. The 420 °C curve (open circles) has been multiplied by a factor 5 in order to ease comparison.

maximized, resulting in enhanced heterogeneous decomposition of TMIn, and efficient heat transfer from the heating element to the carrier gas, and TMIn. It would also result in a more homogeneous temperature profile, which is advantageous for diagnostics. In one design of the reactor the ceramic heater tube was therefore filled with ceramic beads (Si_3N_4, approximately 2 mm diameter) acting as a packed bed for the TMIn flow. Shown in figure 5.1(a) is the 451 nm LIF signal from indium atoms produced by pyrolysis by flowing TMIn through a hot packed bed of silicon nitride beads. The reactor temperature was ramped down from 700 °C to 200 °C over a period of 8 min. At reactor temperatures higher than approximately 600 °C the indium LIF signal increases exponentially with temperature. When ramping the temperature down, there is a steep increase in indium concentration between 300 °C and 550 °C, peaking near 420 °C.

In order to investigate this, the 410 nm excitation laser power was varied between zero and 80 mW. Shown in figure 5.1(b) is the power dependence of the 451 nm indium LIF signal above the reactor, when at two different reactor temperatures. The LIF intensity obtained at 420 °C follows a P^a dependence on laser excitation power P, with an exponent $a \approx 1.8$. At 570 °C the the exponent a is close to unity, or less. An explanation may be found in how atomic indium is generated in each case. At the lower temperature, it can be supposed that some of the indium exists as monomethylindium (MMIn, $InCH_3$) as a result of the stepwise thermal decomposition of TMIn, [52, 53] whereas at the higher temperature this fraction would be significantly smaller. MMIn, which likely has an absorption band in the visible above 400 nm, [54] and a dissociative excited state, could then resonantly absorb a 410 nm photon and dissociate into atomic indium, which can subsequently be excited, causing fluorescence. This would be a (sequential) two-photon process, with a dependence

on excitation power that follows I^2, whereas a single-photon process would be linear in power. With lower gas-phase concentration of MMIn at the higher temperature, and higher concentration of indium atoms, the power dependence is closer to linear.

2 CW photodissociation of TMIn

Since nanowire growth by aerotaxy is a continuous process, it is natural to use a continuous photolysis source. Furthermore, for practical measurements it is desirable to have a compact, robust, stable, and cheaper alternative to high energy pulsed lasers. Alternatives to lasers include excimer lamps and light-emitting diodes (LEDs). Excimer (excited dimer) lamps have similar characteristics to typical glow discharge lamps but emit in the deep ultraviolet. Of the commercially available LEDs the shortest wavelengths available with reasonable output power (a few to a few tens of mW) range from 250 to 260 nm, with a spectral bandwidth in the order of ten nanometer, which is acceptable due to the broad absorption features of many MO precursors, cf. figure 4.1. In order to investigate the feasibility of low-average-power CW photodissociation of TMIn, a deuterium (D_2) lamp (L1314, Hamamatsu) was employed for photodissociation instead of the pulsed laser used in chapter 4. Unlike typical LEDs and excimer lamps, the D_2 lamp has a broad continuum emission spectrum peaking around 200 nm and extending to the visible. Shown in figure 5.2 is a typical emission spectrum. The indium atoms above the reactor were excited using a CW laser at 410 nm, similar to as described in chapter 4, and the non-resonant LIF signal was collected at 451 nm using a CMOS camera, without intensifier (UI-3240CP-NIR-GL, IDS).

Shown in figure 5.3 is the spatially resolved indium PLIF signal at different reactor temperatures, with and without the D_2 lamp. Shown in (a) is the PLIF signal at 600 °C with the D_2 lamp turned off. TMIn is pyrolytically decomposed near the inner walls of the reactor tube, resulting in a conical indium vapor distribution. Shown in (b) is the indium PLIF signal at the same temperature, with the D_2 lamp turned on, resulting in increased produc-

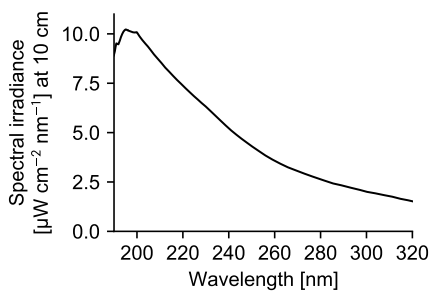

Figure 5.2: Typical emission spectrum of a Hamamatsu L1314 deuterium lamp

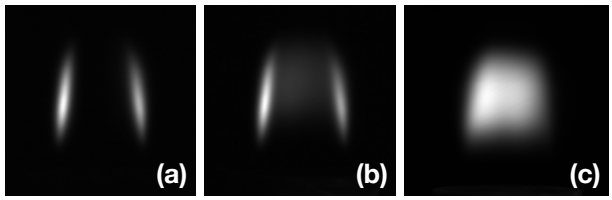

Figure 5.3: Laser induced fluorescence from indium produced by pyrolysis, and by CW photolysis of trimethylindium using a deuterium (D_2) lamp. The images were collected at three different reactor temperatures, with and without the D_2 lamp: **(a)** 600 °C without D_2 lamp, **(b)** 600 °C with D_2 lamp, and **(c)** 200 °C with D_2 lamp. No laser-induced fluorescence was observed at 200 °C without the D_2 lamp. The camera sensitivity setting was the same for all three images.

tion of indium in the central, cooler region. Finally, shown in (c) is the indium PLIF signal with the D_2 lamp turned on, at 200 °C reactor temperature. The lower temperature results in less indium produced by pyrolysis and more from the D_2 lamp. At any temperature the production of indium is the result of a combination of UV photolysis and pyrolysis by the heater tube.

At high temperature, pyrolysis is the main pathway for indium production, whereas at lower temperature photolysis dominates, and the dominating process can be determined by imaging the indium distribution. The fact that a deuterium lamp is sufficient to visibly photodissociate indium is encouraging for future experiments. The lamp could then conceivably be replaced with an array of deep UV LEDs at different wavelengths for increased spectral resolution, lower cost, and a more flexible, robust, and compact setup.

3 Preliminary results of laser ablation of gold nanoparticles with LIF detection of atomic fragments

Combining laser ablation and laser-induced fluorescence can potentially be a highly sensitive technique for optical diagnostics of airborne metal nanoparticles. The general idea is illustrated in figure 5.4. A small amount of vapor ablated from the particles using one laser, and a second laser is used to probe the atomic fragments. Described below is a set of experiments on airborne gold nanoparticles, wherein a pulsed laser was used for ablation of gold nanoparticles in the deep UV, and a dye laser, scanned across a resonance line of atomic gold was used for detecting the ablated gold atoms using LIF. The resulting laser excitation scans exhibit an unusual broadening or splitting of the atomic gold lineshape. Possible explanations include a coupling between the particles and gold atoms, or localized microplasmas, and further investigations of the phenomenon may lead to the development of new in-situ diagnostic techniques for probing the microscopic environment close to in-

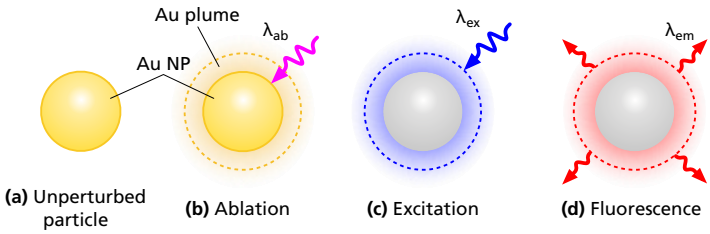

Figure 5.4: Illustration of gold nanoparticle (Au NP) ablation combined with laser-induced fluorescence (LIF) detection of the ablated atomic fragments. **(a)** Gold nanoparticle before excitation; **(b)** gold atoms are ablated from the nanoparticle using a laser with wavelength λ_{ab}; **(c)** a second laser tuned to an absorption line of atomic gold at λ_{ex} is used to excite atoms in the ablated vapor plume; **(d)** the non-resonant laser-induced fluorescence (LIF) emitted by the gold atoms at a third wavelength λ_{em} is collected using a sensitive camera.

dividual airborne metal nanoparticles using optical far field measurements.

3.1 Experimental

Gas-borne gold nanoparticles were generated in a spark discharge, as described in chapter 2, with a 2 mm spark gap and nitrogen as carrier gas. The capacitor charger was operated at 12 kV voltage setpoint and 10 mA charging current setpoint.

Gold atoms were ablated from the particles in open air, downstream of the spark discharge generator, using a pulsed laser at ~225 nm. The inner diameter of the vertical flow tube exit below the optical probe region was 1.5 mm. The ablation beam was generated by the frequency doubled signal beam from an optical parametric oscillator (OPO, model premiScan, GWU), pumped by a Nd:YAG laser at 355 nm (Pro 290, SpectraPhysics). The beam was focused using an $f = 150$ mm fused silica cylindrical lens, forming a horizontal or vertical laser sheet, intersecting the vertical gold nanoparticle flow. Pulse energy at 225 nm was approximately 5 mJ, and pulse duration 10 ns.

The ablated gold atoms were probed using LIF. The probe pulse was generated by the second harmonic of the output from a dye laser (PrecisionScan, Sirah). The probe beam was collimated, and crossed the ablation beam at approximately 15°. The wavelength of the probe laser was scanned over the 242.8 nm absorption line of neutral gold, corresponding to the $6s\ ^2S_{1/2}$ to $6p\ ^2P_{3/2}$ absorption line, resulting in emission of LIF from $^2P_{3/2}$ to $^2D_{5/2}$ at 312 nm. An energy level diagram of neutral gold is shown in figure 2.6. Fluorescence was also observed at 267.6 nm and 627.8 nm, likely due to radiationless transitions to the $6p\ ^2P_{1/2}$ level.

The 312 nm LIF signal was collected perpendicularly to the horizontal probe beam and the vertical particle flow using an intensified CCD camera (ICCD, PI-MAX 2, Princeton Instruments) with a fused silica lens (Nikon, $f = 50$ mm, $f/3.5$). A combination of a band pass filter (BG3, Schott), and an interference filter (320 nm center wavelength, 40 nm bandwidth, Semrock) was used to block elastic scattering. The ICCD gate duration was 30 ns, and the delay between the ablation pulse and the probe pulse was varied between zero and 100 µs.

3.2 Results and analysis

Shown in figure 5.5 (a) and (b) are direct images of the Au LIF inside the nanoparticle flow, using a horizontally focused ablation beam, using (a) no delay, and (b) with the probe pulse delayed 100 µs after the ablation pulse. Shown in (c) is the LIF signal with the ablation beam vertically focused with zero delay between the ablation and probe pulses. The corresponding lineshapes are shown in figure 5.5 (d) and (e). Specifically, integrating the regions above and below the dashed line in (c) result in different absorption lineshapes, as shown in (e).

At the nanosecond timescale, gold atoms are photo-thermally ablated by evaporation. [55] Fragments, clusters and neutral excited and ionized atomic gold are evaporated from the particles, at a rate determined by the laser intensity. If the resulting particle cloud or plasma is sufficiently dense, it may shield the particles from further absorption, and possibly absorb energy from the field (inverse Bremsstrahlung), causing further plasma heating.

The excitation scans exhibit broad features, which appears to be dependent on the intensity of the ablation laser beam. In general, observed linewidths range from 0.01 to 0.05 nm. Given the shape of the observed lineshape, the most straight forward explanation for the broadening would be similar to what could be expected in a plasma, i.e., a combination of effects caused by phase-changing collisions with perturbing particles, and longer-range interactions with quasi-stationary, massive particles due to Stark effect in the case of charged particles, and resonance broadening or Van der Waals broadening for neutral species. Besides broadening, there is also a splitting, or shift, of the observed spectral line. Zeeman splitting has been observed in laser-induced plasmas. [56] Finally, the laser will broaden the Doppler-limited absorption line, but both instrumental and Doppler broadening are negligible compared to the observed effects, and provide no explanation for the asymmetry. Self-absorption may result in a depressed line center. The absence of any visible broadband emission (Bremsstrahlung), or emission from anything other than neutral gold, implies that any plasma is likely relatively cool or confined to a small volume, like the surface of each particle.

The authors of Ref. [57] observed the Stark width (FWHM) of the 242.8 nm neutral gold line of 0.008 nm in emission, in a helium plasma at 16 800 K, estimating that any contribution from Doppler, Van der Waals and resonance broadening to be at least one order of magnitude smaller than Stark broadening. Moreover, the authors of Ref. [58] reported line widths in the range of 1 to 0.5 nm for several Au I emission lines (not including the 243 nm line) in a laser-induced plasma. Asymmetry was observed up to 1 µs following breakdown.

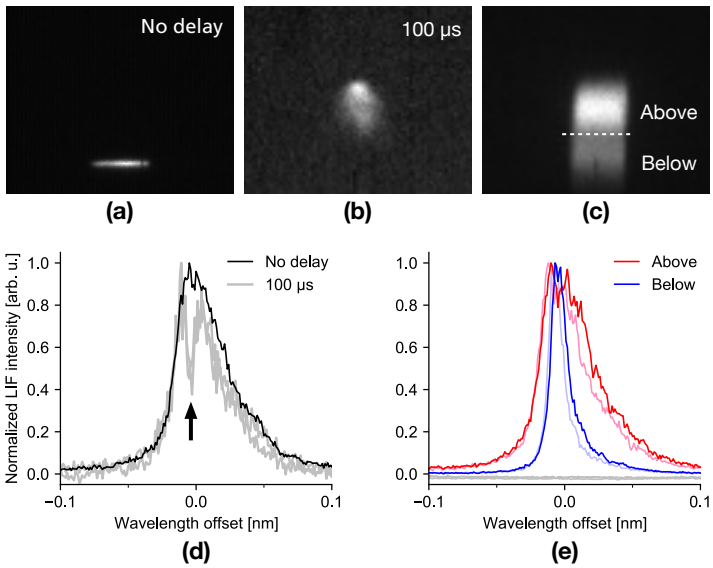

Figure 5.5: **Upper row:** Direct images of laser-induced fluorescence from ablated gold atoms in the nanoparticle flow, approximately 5 mm above the ~1.5 mm inner diameter exit tube. In **(a)** and **(b)** a horizontal ablation laser sheet was employed. The delay between the ablation pulse and the probe pulse, was (a) zero, and (b) 100 µs. **(c)** Laser-induced fluorescence collected using a vertically oriented ablation laser sheet using zero delay delay between the ablation and probe pulses. The corresponding excitation scans are shown in (d) and (e). **Lower row:** Au LIF lineshapes at 312 nm, when excited at 243 nm, collected with vertically focused ablation beam. The LIF intensity has been normalized. **(d)** Influence of delay between ablation pulse and probe pulse on lineshape. The black curve was collected at zero delay between the ablation and the probe pulses. The two gray curves represent two different excitation scans, collected with 100 µs delay between the ablation and probe pulses, and with the ablation laser horizontally focused. Note the dip near the line center. **(e)** Influence of ablation beam intensity on the lineshape. Due to inhomogeneities in the beam profile of the ablation laser, the intensity varies over the laser sheet. The solid red and blue curves show the respective lineshapes above and below the dashed line in (c), at zero delay between the ablation and probe pulses. The lighter red and blue curves were collected with a 1 µs delay between the ablation and probe pulses. The horizontal gray lines near zero intensity are the collected lineshapes with either the ablation beam or the probe beam blocked, or the Au NP flow turned off. The ablation laser was vertically focused.

3.3 Summary and conclusions

The observed absorption lineshapes of atomic gold ablated from nanoparticles are in the range of 1–2 orders wider than what can be expected under ambient conditions. Furthermore, the profiles exhibit asymmetry, with a tail toward the red, and sometimes several peaks are observed during the same laser scan. In general, the magnitude of the splitting correlates with the broadening, i.e., they may be caused by the same physical effect. The observed linewidth appears to be sensitive to intensity and possibly to overlap between ablation and probe beams. The fact that the observable quantity (frequency shift and lineshape broadening) is in the spectral domain means that a high level of precision is potentially achievable using high-resolution laser spectroscopy.

With the limited amount of data available, one explanation for the observed lineshapes is Stark broadening caused by highly charged particles. The effects are still present at least 100 µs following the ablation pulse, with the envelope mostly the same but with a dip in the lineshape.

The particle size distribution, number concentration and the charge distribution of the produced particles are generally unknown quantities. In general, more experiments are required in order to confirm the nature of the observed effects, under better controlled, and varied, conditions; e.g., experiments performed with known particle number concentration and size distribution, under variation of ablation or excitation pulse energy (intensity). Further measurements are necessary in order to determine whether the observed frequency shifts are positive or negative; ideally the non-broadened Au line would be used as reference, measured simultaneously, e.g., in a stable flame, furnace, or discharge cell.

4 Preliminary results of optical monitoring of the nanoparticle alloying process

In gold-seeded nanowire growth, the trunk of the wire grows from an alloy between the gold particles and the atomic indium provided by, e.g., TMIn. The gas-phase alloying process can therefore be seen as the first step in the wire growth. The aim with these experiments was to investigate gas-phase Au–In alloying using optical diagnostic techniques, and to evaluate the possibility of optically influencing the alloying process. By monitoring the process in real-time, in-situ, the growth conditions can be optimized without time-consuming batch processing.

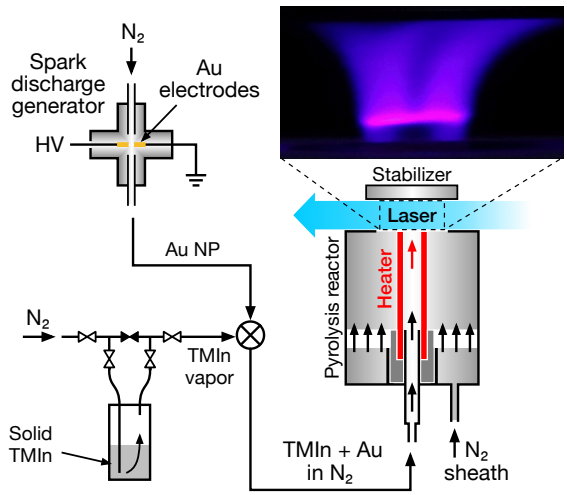

Figure 5.6: Experimental setup for optical diagnostics on gas-phase Au–In alloying. The vacuum pumps used for purging the metal-organic vapor delivery system and the spark discharge system have been omitted from the figure. Shown in the inset is the laser-induced fluorescence from indium atoms excited at 410 nm.

4.1 Experimental

Shown in figure 5.6 is the experimental setup which combines the spark discharge nanoparticle generator described in Paper I, and the metal-organic vapor delivery system and flow reactor described in Paper III. The TMIn and gold nanoparticle flows were mixed before being carried in nitrogen to the reactor and heated. The optical setup is shown schematically in figure 5.7, and is similar to that used for investigating the pyrolysis and photolysis of TMIn in Paper III, with the main difference that the pulsed photolysis laser used in Paper III was replaced with a pulsed Nd:YAG laser generating 355 nm light (Brilliant-B, Quantel) instead of 213 nm. Pulse energy at 355 nm was approximately 2.5 mJ. The 355 nm wavelength does not coincide with the known absorption spectrum of TMIn, which peaks around 213 nm. [59] The wavelength was chosen to only interact directly with solid particles, thereby any pulsed laser ablation of the particles resulting in an increase in the indium signal would be an indication of the presence of Au–In particles.

For imaging of the ES of particles a CW 532 nm DPSS laser (Roithner Lasertechnik) was employed with an output power of approximately 300 mW. The beam was expanded to a 19 mm vertical laser sheet, intersecting the vertical TMIn and gold nanoparticle flow between the reactor and flow stabilizer. For LIF of indium, second harmonic of the Ti:sapphire laser described in Sec. 1.3 was used, and the 410 nm beam was expanded in the same way as the ES sheet. Output power at 410 nm was approximately 25 mW. The ES and LIF beam paths were overlapped for convenience and mostly share the same optics, but were not em-

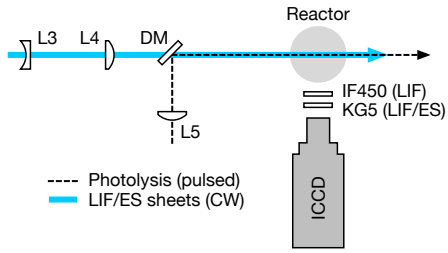

Figure 5.7: Optical setup for particle alloying measurements. The blue solid line indicates the 410 nm and 532 nm laser sheets used for laser-induced fluorescence (LIF) of indium, and elastic scattering from particles (ES), respectively. The dashed line indicates the 355 nm pulsed ablation beam.

ployed simultaneously. The ES and LIF were imaged using an intensified CCD (ICCD) camera (PIMAX 2, Princeton Instruments). For indium LIF measurements, a narrowband interference filter centered on 450 nm was used for blocking elastic laser light.

4.2 Results and analysis

Shown in figure 5.8 are some results from elastic scattering by gold nanoparticles, with and without TMIn in the flow, at reactor temperatures from 600 to 750 °C. No ablation laser was used. The increased scattering with TMIn in the flow compared to just gold nanoparticles indicates that at least the TMIn is condensing on the gold particles. The difference increases slightly with temperature, and at 750 °C reactor temperature the scattering intensity is a factor 2–3 higher with TMIn in the flow compared to just gold nanoparticles.

Shown in figure 5.9 is the integrated indium LIF signal, when starting and stopping the spark discharge generator at 0 s, with TMIn flowing. No ablation laser was used. The gas flow through the spark discharge generator was held constant during the experiments, and only the high voltage to the discharge generator was turned off or on, respectively. The results indicate about 10 to 15 % decrease in indium LIF signal at 750 °C reactor temperature with gold nanoparticles in the flow, which could indicate the loss of free indium atoms due to condensation of In, TMIn or some intermediate species on the gold nanoparticles.

Shown in figure 5.10 are images collected with only the 355 nm ablation laser, without the 410 nm or 532 nm laser sheets, and with both gold nanoparticles and TMIn in the flow. The reactor temperature was varied from 600 to 750 °C. Above 600 °C strong In^* emission is observed at short delays after the ablation pulse, indicating that somewhere between 600 °C and 650 °C the ablated particles contain a large amount of indium. Below 600 °C the indium emission is negligible.

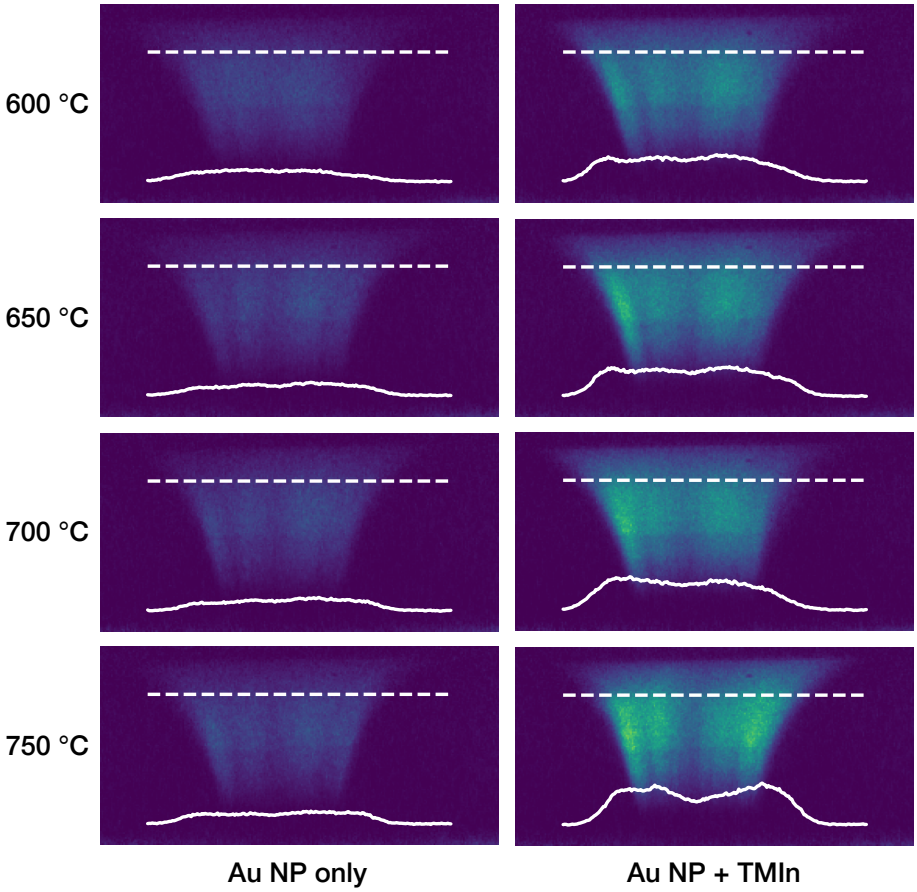

Figure 5.8: False color elastic scattering from gold nanoparticles at 750 °C reactor temperature, without TMIn in the flow (left), and with TMIn (right). The excitation laser wavelength was 532 nm, and the beam was expanded to a 19 mm tall laser sheet, intersecting the gas flow above the reactor. The solid curves indicates the scattering intensity along the broken lines.

Finally, shown in figure 5.11 is the elastically scattered light from a vertical flow of gold nanoparticles, intersected by the ablation laser, indicating a hole-burning effect.

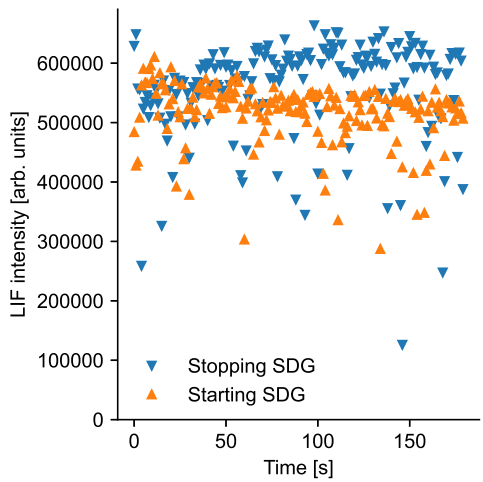

Figure 5.9: Time-resolved response of the indium laser-induced fluorescence (LIF) signal when stopping or starting the gold nanoparticle generator in the presence of TMIn. Reactor temperature was 750 °C. The upwards-pointing (orange) triangles indicate the LIF signal when the high voltage was turned on at 0 s, whereas the downwards-pointing (blue) triangles indicate the LIF signal when the high voltage was turned off at 0 s.

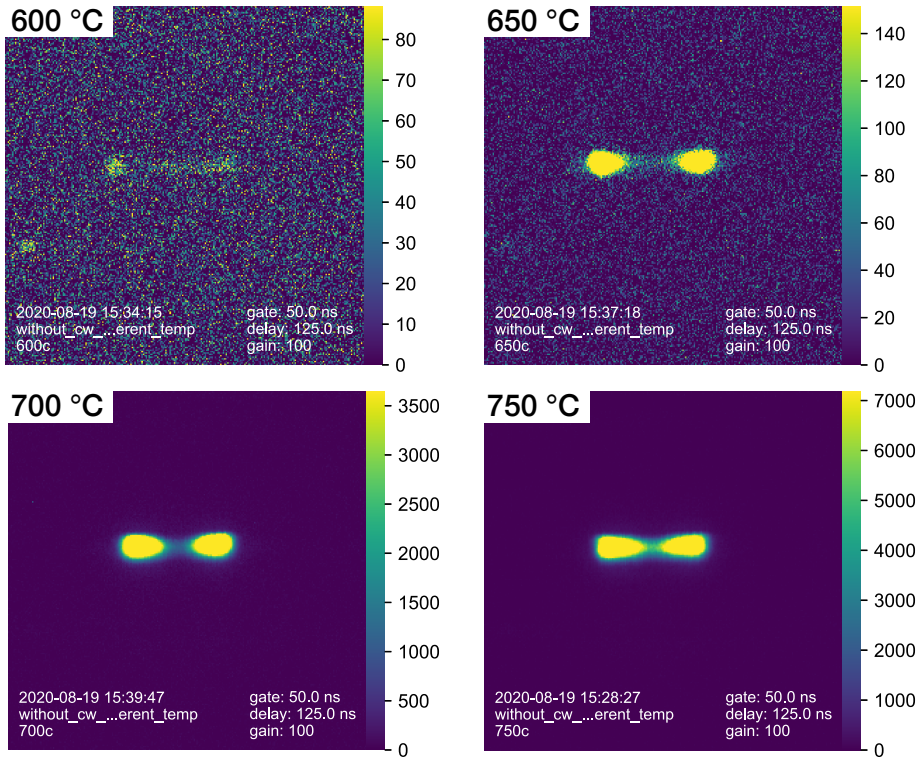

Figure 5.10: Pulsed laser ablation of gold nanoparticles in the presence of TMIn, at different reactor temperatures. A 450 nm bandpass filter was used to filter out the In^* emission at 451 nm. The stronger signal near the edges of the TMIn flow is due to the more efficient heating near the inner walls of the heating element. The reactor temperature is indicated in each figure. Note the different intensity scales.

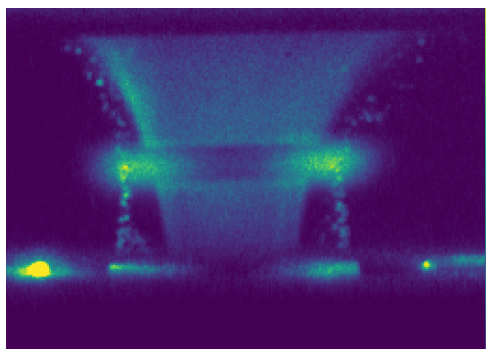

Figure 5.11: Elastic scattering of gold nanoparticles mixed with TMIn at 600 °C reactor temperature. A 355 nm ablation beam passes through the flow, resulting in a hole-burning effect.

4.3 Summary and conclusions

The ES measurements without the ablation laser indicate that the gold nanoparticles grow in size as a result of mixing with TMIn, and the effect is stronger at higher temperatures. The LIF measurements without the ablation laser indicate that introducing gold particles into the TMIn flow slightly reduces the indium concentration, and that TMIn or atomic indium lost to condensation on the gold particles.

The results with TMIn and gold nanoparticles in the flow, and with only the ablation laser, indicate that the gold particles contain a significant amount of indium at reactor temperatures above 650 °C reactor temperature. This could be due to increased diffusion of indium into the gold particles at the higher temperatures, allowing each gold particle to hold a larger amount of indium than is possible only from surface condensation of TMIn.

It can be concluded that laser ablation at 355 nm is a feasible technique for studying the gas-phase alloying process between gold nanoparticles and indium provided by TMIn. Further investigations should include combination of ablation with laser induced fluorescence detection of the ablated fragments, which should increase the sensitivity and specificity of the method considerably.

Chapter 6

Summary and outlook

The work described in this thesis constitutes the first steps towards applying laser-diagnostic techniques to two important fields: aerosol metal nanoparticle generation by spark discharge and aerosol-phase metal particle-seeded functional nanowire growth (aerotaxy). Aerotaxy is one of the most promising technologies for producing cost-effective semiconductor components at an industrial scale.

In Paper I, two-photon laser-induced fluorescence was employed to visualize the gold atom plume ablated from gold electrodes during discharge. The distribution and concentration of gold are used as a starting point for the modeling of the particle growth process, [22] resulting in a better understanding, and guiding the development of more efficient aerosol generators. Is it easy to see how the method could be improved to two-dimensional imaging of the ablated atom plume if higher laser intensity could be achieved. In the paper, gold was used for demonstrating the general approach, due to its importance as seed-particles for nanowire growth, however, the method could be easily extended to other materials.

In Paper II, the gas-borne gold particles generated in the discharge were characterized using in-situ optical methods. For the first time, the photoluminescence of airborne gold nanoparticles was detected, and the quantum efficiency was determined. However, there are still many questions remaining regarding the origin, characteristics, and material dependence of the photoluminescence. The results of imaging measurements revealed structures that indicate the possibility of single-particle imaging, if the imaging resolution were increased. The particles were excited at 532 nm. Exciting at other wavelengths and measuring the spectrally resolved photoluminescence emission could help explain the shape of the photoluminescence signal and its relation to the plasmon resonance. In Paper II the particles were generated by a spark discharge generator, resulting in agglomerates, whereas Mie theory assumes spherical particles. Better controlled conditions could be achieved by

using size selected particles. If the photoluminescence follows the Mie extinction curve, as suggested, [29] this would help minimize any smearing due to superposition of the photoluminescence spectra from different size groups. Furthermore it may help explain why the photoluminescence signals of copper or silver are so low compared to gold. Adding a small amount of H_2 to the carrier gas mixture may help avoid oxidation, [60] which may have reduced any plasmonic response from easily oxidized materials.

In Paper III, the pyrolysis and photolysis of trimethylindium (TMIn), an important indium precursor for group III–V compound semiconductor growth, was studied optically. The concentration of indium atoms generated by pyrolysis and photolysis was studied quantitatively, while spatially, and temporally resolved. Similar approaches should work for other common precursors like TMGa, and TMAl. Photolytic growth of particles or wires due to photolysis or laser heating of seed particles may be one way to avoid parasitic reactions. NH_3 may be a suitable alternative to AsH_3 or PH_3, in combination with, e.g., TMGa, for demonstrating laser-catalyzed wire growth, due to its relatively better-characterized spectroscopic properties, and possibility for better spectral selectivity. The relatively high decomposition temperature of NH_3 is attractive because then, TMGa, having broad absorption spectrum could be decomposed pyrolytically, while NH_3 could be selectively photolyzed using a suitable wavelength. Other seed particles may then be required than gold. [61]

Finally, in chapter 5 the first stage of nanowire growth, i.e., the gas-phase alloying between gold nanoparticles and indium was studied using a combination of pulsed laser ablation of the alloy particles and CW detection of alloy fragments using laser-induced fluorescence. Preliminary results indicate a strong temperature dependence on the indium content of the alloy particles, which increases sharply above 600 °C. Preliminary results of lineshape measurements of gold ablated from airborne gold nanoparticles resulted in broadened lineshapes suggesting the possibility to probe the micro-environment surrounding the particles using laser spectroscopy.

Chapter 7

Acknowledgments

As of this writing, it's getting late—well, early—and this thesis is about to be sent to the printer. Where to begin? There are too many people that I would like to thank that have contributed in different ways to making the division of Combustion Physics such a nice place to work.

First of all, I would like to express my deepest gratitude to my main supervisor Zhongshan for being given the opportunity to do my PhD studies at the division. Without your broad experience, enthusiasm, support and encouragement I would not have made it this far. I have especially enjoyed the a generous amount of freedom I have been granted over the years. I also want to thank my co-supervisor Marcus for your support, and your leadership.

A special thank you to Minna and Cecilia for assistance with practical things, and to Igor for help with various technical issues.

I would like to express my sincere thanks to my colleagues in the aerosol group: Martin, Knut, and Markus, and others. Thank you for the collaboration, and thank you Calle, Linus, Robert, Elena for helping out in the lab. I am grateful to Bengt and Sören for all the help in the workshop.

Over the years I have had a shocking number of office mates: Tomas, I was always impressed with your dedication to your work. Chengdong, your broad knowledge and intelligence is inspiring. I hope you are doing well. Shishi and David, I wish you continued success in your studies.

References

[1] R. M. Osgood, Jr., "Laser microchemistry and its application to electron-device fabrication," Annu. Rev. Phys. Chem. **34**, 77–101 (1983).

[2] W. Richter, P. Kurpas, R. Lückerath, M. Motzkus, and M. Waschbüsch, "Gas phase studies of MOVPE by optical methods," J. Cryst. Growth **107**, 13–25 (1991).

[3] K. Deppert and L. Samuelson, "Self-limiting transformation of monodisperse Ga droplets into GaAs nanocrystals," Appl. Phys. Lett. **68**, 1409–1411 (1996).

[4] M. Heurlin, M. H. Magnusson, D. Lindgren, M. Ek, L. R. Wallenberg, K. Deppert, and L. Samuelson, "Continuous gas-phase synthesis of nanowires with tunable properties," Nature **492**, 90–95 (2012).

[5] A. Schmidt-Ott, ed., *Spark Ablation: Building Blocks for Nanotechnology* (Jenny Stanford Publishing Pte. Ltd., 2020).

[6] E. M. Bazelyan and Y. P. Raizer, *Spark Discharge* (CRC Press, Boca Raton, New York, 1997).

[7] N. S. Tabrizi, M. Ullmann, V. A. Vons, U. Lafont, and A. Schmidt-Ott, "Generation of nanoparticles by spark discharge," J. Nanopart. Res. **11**, 315–332 (2009).

[8] F. Llewellyn Jones, "Electrode erosion by spark discharges," Brit. J. Appl. Phys. **1**, 60–65 (1950).

[9] J. W. Arblaster, "Thermodynamic properties of gold," Phase Equilib. Diffus. **37**, 229–245 (2016).

[10] J. M. Palomares, A. Kohut, G. Galbács, R. Engeln, and Z. Geretovszky, "A time-resolved imaging and electrical study on a high current atmospheric pressure spark discharge," J. Appl. Phys. **118**, 233305 (2015).

[11] N. Konjević, "Plasma broadening and shifting of non-hydrogenic spectral lines: present status and applications," Phys. Rep. **316**, 339–401 (1999).

[12] T. Shirai, J. Reader, A. E. Kramida, J. Sugar, and NIST ASD Team, "NIST Atomic Spectra Database (ver. 5.0)," Online (2012). Retrieved April 1, 2013.

[13] A. P. Thorne, U. Litzén, and S. Johansson, *Spectrophysics* (Media-Tryck, Lund, 2007).

[14] A. Kohut, G. Galbács, Z. Márton, and Z. Geretovszky, "Characterization of a copper spark discharge plasma in argon atmosphere used for nanoparticle generation," Plasma Sources Sci. Technol. **26**, 045001 (2017).

[15] H. R. Griem, "Validity of local thermal equilibrium in plasma spectroscopy," Phys. Rev. **131**, 1170–1176 (1963).

[16] E. Carbone and S. Nijdam, "Thomson scattering on non-equilibrium low density plasmas: principles, practice and challenges," Plasma Phys. Control. Fusion **57**, 014026 (2015).

[17] D. C. Price, "Empirical lineshape for computer fitting of spectral data," Aust. J. Phys. **34**, 51–56 (1981).

[18] R. J. Dewhurst, G. J. Pert, and S. A. Ramsden, "Picosecond triggering of a laser-triggered spark gap," J. Phys. D Appl. Phys. **5** (1972).

[19] A. H. Guenther and J. R. Bettis, "The laser triggering of high-voltage switches," J. Phys. D Appl. Phys. **11**, 1577–1613 (1978).

[20] R. A. Dougal and P. F. Williams, "Fundamental processes in laser-triggered electrical breakdown of gases," J. Phys. D Appl. Phys. **17**, 903–918 (1984).

[21] N. S. Tabrizi, Q. Xu, N. M. van der Pers, U. Lafont, and A. Schmidt-Ott, "Synthesis of mixed metallic nanoparticles by spark discharge," J. Nanopart. Res. **11**, 1209–1218 (2009).

[22] J. Feng, L. Huang, L. Ludvigsson, M. E. Messing, A. Maisser, G. Biskos, and A. Schmidt-Ott, "General approach to the evolution of singlet nanoparticles from a rapidly quenched point source," J. Phys. Chem. C **120**, 621–630 (2016).

[23] N. A. Fuchs, "On the stationary charge distribution on aerosol particles in a bipolar ionic atmosphere," Geofisica pura e applicata **56**, 185–193 (1963).

[24] A. Wiedensohler, "An approximation of the bipolar charge distribution for particles in the submicron size range," J. Aerosol Sci. **19**, 387–389 (1988).

[25] A. Mooradian, "Photoluminescence of metals," Phys. Rev. Lett. **22**, 185–187 (1969).

[26] G. T. Boyd, Z. H. Yu, and Y. R. Shen, "Photoinduced luminescence from the noble metals and its enhancement on roughened surfaces," Phys. Rev. B **33**, 7923–7936 (1986).

[27] P. Apell and R. Monreal, "Photoluminescence of noble metals," Phys. Scripta **38**, 174–179 (1988).

[28] M. B. Mohamed, V. Volkov, S. Link, and M. A. El-Sayed, "The 'ligtning' gold nanorods: fluorescence enhancement of over a million compared to the gold metal," Chem. Phys. Lett. **317**, 517–523 (2000).

[29] E. Dulkeith, T. Niedereichholz, T. A. Klar, J. Feldmann, G. von Plessen, D. I. Gittins, K. S. Mayya, and F. Caruso, "Plasmon emission in photoexcited gold nanoparticles," Phys. Rev. B **70**, 205424 (2004).

[30] L. Jauffred, S. M.-R. Taheri, R. Schmitt, H. Linke, and L. B. Oddershede, "Optical trapping of gold nanoparticles in air," Nano lett. **15**, 4713–4719 (2015).

[31] L. Jauffred, "Why not use thermal radiation for nanothermometry," Appl. Opt. **57**, 9508–9511 (2018).

[32] J. Hernandez-Rueda, A. de Beurs, and D. van Oosten, "Ultrafast laser ablation of trapped gold nanoparticles," Opt. Lett. **44**, 3294–3297 (2019).

[33] K. L. Kelly, E. Coronado, L. L. Zhao, and G. C. Schatz, "The optical properties of metal nanoparticles: The influence of size, shape, and dielectric environment," J. Phys. Chem. B **107**, 668–677 (2003).

[34] V. Amendola, R. Pilot, M. Frasconi, O. M. Maragò, and M. A. Iatì, "Surface plasmon resonance in gold nanoparticles: a review," J. Phys.: Condens. Matter **29**, 203002 (2017).

[35] H. Goldenberg and C. J. Tranter, "Heat flow in an infinite medium heated by a sphere," Brit. J. Appl. Phys **3**, 296–298 (1952).

[36] P. Grua, J. P. Morreeuw, H. Bercegol, G. Jonusauskas, and F. Vallée, "Electron kinetics and emission for metal nanoparticles exposed to intense laser pulses," Phys. Rev. B **68**, 035424 (2003).

[37] M. Strasser, K. Setoura, U. Langbein, and S. Hashimoto, "Computational modeling of pulsed laser-induced heating and evaporation of gold nanoparticles," J. Phys. Chem. C **118**, 25748–25755 (2014).

[38] J. R. Sambles, "An electron microscope study of evaporating gold particles: the Kelvin equation for liquid gold and the lowering of the melting point of solid gold particles," Proc. R. Soc. A. **324**, 339–351 (1971).

[39] M. A. Asoro, D. Kovar, and P. J. Ferreira, "*In situ* transmission electron microscopy observations of sublimation in silver nanoparticles," ACS Nano (2013).

[40] H. L. Partner, J. Zoll, A. Kuhlicke, and O. Benson, "Printed-circuit-board linear Paul trap for manipulating single nano- and microparticles," Rev. Sci. Instrum. **89**, 083101 (2018).

[41] F. G. Major, V. N. Gheorghe, and G. Werth, *Charged Particle Traps* (Springer, Berlin Heidelberg, 2005).

[42] G. Werth, V. N. Gheorghe, and F. G. Major, *Charged Particle Traps II* (Springer, Berlin Heidelberg, 2009).

[43] C. F. Bohren and D. R. Huffman, *Absorption and Scattering of Light by Small Particles* (Wiley, Weinheim, 1983).

[44] H. C. van de Hulst, *Light Scattering by Small Particles* (Dover, New York, 1981).

[45] T. Beuermann and M. Stuke, "Photolysis of group III (Al, Ga, In) trimethyl compounds: detection of organic photofragments CH_3 and C_2H_6 by picosecond laser mass spectroscopy," Chem. Phys. Lett. **178**, 197–203 (1991).

[46] E. V. Gurentsov, "UV laser synthesis of nanoparticles in the gas phase," Kinet. Catal. **58**, 233–254 (2017).

[47] D. Kaur, A. M. de Souza, J. Wanna, S. A. Hammad, L. Mercorelli, and D. S. Perry, "Multipass cell for molecular beam absorption spectroscopy," Appl. Opt. **29**, 119–124 (1990).

[48] P. F. Moulton, "Spectroscopic and laser characteristics of Ti:Al_2O_3," Opt. Soc. Am. B **3**, 125–133 (1986).

[49] T. W. Hänsch and B. Couillaud, "Laser frequency stabilization by polarization spectroscopy of a reflecting reference cavity," Opt. Commun. **35**, 441–444 (1980).

[50] C. B. Alcock, V. P. Itkin, and M. K. Horrigan, "Vapour pressure equations for the metallic elements: 298–2500 K," Can. Metall. Quart. **23**, 309–313 (1984).

[51] D. V. Shenai-Khatkhate, R. L. D. Jr., and R. A. Ware, "Accurate vapor pressure equation for trimethylindium in OMVPE," J. Cryst. Growth **310**, 2395–2398 (2007).

[52] M. G. Jacko and S. J. W. Price, "The pyrolysis of trimethylindium," Can. J. Chemistry **42**, 1198–1205 (1964).

[53] C. A. Larsen and G. B. Stringfellow, "Decomposition kinetics of OMVPE precursors," J. Cryst. Growth **75**, 247–254 (1986).

[54] C. Park, W.-S. Jung, Z. Huang, and T. J. Anderson, "*In situ* Raman spectroscopic studies of trimethylindium pyrolysis in an OMVPE reactor," J. Mater. Chem. **12**, 356–360 (2002).

[55] D. Bäuerle, *Laser Processing and Chemistry* (Springer, Berlin, Heidelberg, 2011), 4th ed.

[56] E. A. McLean, J. A. Stamper, C. K. Manka, H. R. Griem, D. W. Droemer, and B. H. Ripin, "Observation of magnetic fields in laser-produced plasma using the Zeeman effect," Phys. Fluids **27**, 1327–1335 (1984).

[57] S. Djeniže, A. Srećković, S. Bukvić, and N. Vitas, "The Ag I and Au I resonance line broadening in helium plasma," Z. Naturforsch. **61a**, 491–498 (2006).

[58] B. Német and L. Kozma, "Time-resolved line shape studies of Nd:YAG laser-induced microplasmas arising from gold surfaces," Fresen. J. Anal. Chem. **355**, 904–908 (1996).

[59] V. Woods and N. Dietz, "InN growth by high-pressure chemical vapor deposition: Real-time optical growth characterization," Mater. Sci. Eng. B **127**, 239–250 (2006).

[60] R. T. Hallberg, L. Ludvigsson, C. Preger, B. O. Mueller, K. A. Dick, and M. E. Messing, "Hydrogen-assisted spark discharge generated metal nanoparticles to prevent oxide formation," Aerosol Sci. Tech. **52**, 347–358 (2018).

[61] X. Duan and C. M. Lieber, "Laser-assisted catalytic growth of single crystal GaN nanowires," J. Am. Chem. Soc. **122**, 188–189 (2000).

Chapter 8

Scientific publications

Co-authors are abbreviated as follows:
Zhongshan Li (ZSL), Marcus Snellman (MS).

Paper I: Optical measurements in a spark discharge plasma for gold nanoparticle synthesis

The investigation of a spark discharge designed for metal nanoparticle generation using in-situ optical measurements was reported. The operational conditions of the spark discharge were characterized by monitoring the temporally resolved current and voltage profiles, and the plasma emission spectroscopy was recorded and analysis to obtained the real time plasma temperature and free-electron concentration. The spatially and temporally resolved distribution of gold atoms was investigated using a combined two-photon laser induced fluorescence imaging and high-resolution absorption spectroscopy.

I planned and performed the experiments. I performed the data analysis and prepared the manuscript with input from the co-authors.

Paper II: Airborne gold nanoparticle detection using photoluminescence excited with CW laser

The observation of photoluminescence emission from airborne gold, silver and copper nanoparticles was reported. A continuous wave 532 nm laser was employed for excitation. Photoluminescence from gold nanoparticles carried in a nitrogen gas flow were detected both spectrally resolved and directly imaged in-situ using an intensified CCD camera. The

simultaneously detected Raman signal from the nitrogen molecules enables quantitative estimation of the photoluminescence quantum yield of the gold nanoparticles. As far as we are aware, this is the first observation of photoluminescence from metal nanoparticles carried in a gas flow and it provides a potential tool for operando imaging of metal nanoparticles in aerosol reactions.

I planned and performed the experiments. I performed the particle sampling measurements together with MS. I performed the data analysis and prepared the manuscript with input from the co-authors.

Paper III: Optical diagnostics on trimethylindium pyrolysis and photolysis for functional nanoparticle generation

The pyrolysis and photolysis processes of trimethylindium (TMIn) were studied using optical diagnostic techniques, aiming at an in-depth understanding of the governing chemistry and optimization of aerosol-based (aerotaxy) nanowire growth processes. A flow reactor simulating the aerotaxy process with special consideration given to optical access was built to provide the chemical environment to allow in-situ optical measurements on the pyrolysis of TMIn. By probing a resonant transition of indium atom, high resolution laser absorption and laser-induced fluorescence spectroscopy were applied to obtain the atomic indium concentration at different chosen conditions in a spatially and temporally resolved manner. A 213 nm pulsed laser was employed to induce photolytic dissociation of TMIn vapor under chosen conditions. The results indicate that quantitative measurements of indium atoms are feasible. The photolytic dissociation of TMIn vapor with an UV laser turn out to be a promising method in generating substantial chemical effects, indicated by the generation of visible clouds of particles, and high concentration of indium atoms, far beyond the amount generated pyrolytically at the temperature window typically adopted for aerotaxy.

I planned and performed the experiments together with ZSL. I performed the data analysis and prepared the manuscript with input from the co-authors.